



## 저작자표시-비영리-변경금지 2.0 대한민국

이용자는 아래의 조건을 따르는 경우에 한하여 자유롭게

- 이 저작물을 복제, 배포, 전송, 전시, 공연 및 방송할 수 있습니다.

다음과 같은 조건을 따라야 합니다:



저작자표시. 귀하는 원저작자를 표시하여야 합니다.



비영리. 귀하는 이 저작물을 영리 목적으로 이용할 수 없습니다.



변경금지. 귀하는 이 저작물을 개작, 변형 또는 가공할 수 없습니다.

- 귀하는, 이 저작물의 재이용이나 배포의 경우, 이 저작물에 적용된 이용허락조건을 명확하게 나타내어야 합니다.
- 저작권자로부터 별도의 허가를 받으면 이러한 조건들은 적용되지 않습니다.

저작권법에 따른 이용자의 권리는 위의 내용에 의하여 영향을 받지 않습니다.

이것은 [이용허락규약\(Legal Code\)](#)을 이해하기 쉽게 요약한 것입니다.

[Disclaimer](#)

공학박사학위논문

# 종이 접기 구조 기반 지름 가변형 휠의 설계 및 제작

Design and Fabrication of Variable Diameter Wheel based  
on Origami Structure

2017 년 2 월

서울대학교 대학원

기계항공공학부

이 대 영

## **Abstract**

# **Design and Fabrication of Variable Diameter Wheel based on Origami Structure**

Dae-Young Lee

Department of Mechanical and Aerospace Engineering

The Graduate School

Seoul National University

A wheel-drive mechanism is simple, stable, and efficient, but its mobility in unstructured terrain is seriously limited. Employing a deformable wheel is one way to increase the mobility of a wheel-drive robot. By changing the radius of its wheels, the robot is able to pass over not only high steps but also narrow gaps. The thesis propose a novel design of a variable-diameter wheel using an origami-based soft robotics design approach. Soft robots attain infinite degrees of freedom from the soft materials of which they are made (e.g., elastomer and fabric), thereby achieving unique characteristics: dexterity in motion, deformability, and adaptability to environments. Using soft materials for a variable-diameter wheel accompanies two advantages – high deformability and ability to absorb impacts, but inadequate stiffness and excessive degrees of freedom can impede a wheel’s functionality. The key idea is to overcome these

deficiencies by making the wheel structure from a soft material to which an origami pattern has been applied, which reduces the material's excessive degrees of freedom and increases the structure's stiffness.

The proposed design provides three key advantages. First, the structure can be built without many mechanical parts or a complex assembly process. Second, an origami structure can have high stiffness and impact capacity compared to its weight. An origami structure is composed of compliant folding parts and facets, so the whole structure can perform as a shock absorber. Third, an origami structure is scalable. The structure generates a joint by folding, and this reduces friction between links. The simplified assembly process using origami structures reduces the difficulty in assembling small-scale parts.

The thesis presents a design and fabrication method of the transformable wheel and provides a comprehensive analysis of the wheel structure. Also, the thesis contains the robot design with the wheel transformation mechanism. The wheel's diameter can change from 30 mm to 68 mm, and it is light weight at about 9.7 g. Although composed of soft materials (fabrics and films), the wheel can bear more than 400 times its weight. The robot was able to change the wheel's radius in response to terrain conditions, allowing it to pass over a 50-mm gap when the wheel is shrunk and a 50-mm step when the wheel is enlarged.

**Keywords:** Deformable wheel, Transformable wheel, Origami wheel, Origami structure, Soft robot, Patterned composite

**Student Number:** 2013-30950

# Contents

<b>Abstract .....</b>	<b>i</b>
<b>Contents .....</b>	<b>iii</b>
<b>List of Tables.....</b>	<b>v</b>
<b>List of Figures.....</b>	<b>v</b>
<b>Nomenclature .....</b>	<b>xi</b>
<b>Chapter 1 Introduction .....</b>	<b>1</b>
1.1 Motivation.....	1
1.1.1 Transformable Wheel Mechanism.....	1
1.1.2 Soft Robotic Design Approach.....	2
1.1.3 Origami Inspired Design Approach.....	3
1.2 Research Objectives and Contributions .....	3
1.3 Research Overview .....	5
<b>Chapter 2 Variable-Diameter Wheel Design.....</b>	<b>6</b>
2.1 Origami Pattern Design for Variable-diameter Wheel.....	6
2.1.1 Rolled-up Compliant Wheel.....	6
2.1.2 Spiral Foldable Pattern .....	8
2.1.3 Modified Waterbomb Tessellation Pattern .....	10
2.2 Structure Analysis and Improvement .....	14
2.2.1 Kinematic Analysis .....	14
2.2.2 Hybrid Pattern Design.....	30
2.2.3 Design Optimization .....	31
2.3 Wheel Grouser Design.....	34

<b>Chapter 3 Wheel Structure Fabrication .....</b>	<b>36</b>
3.1 Pattern Embedded Composite .....	36
3.2 PET Patterning on Mesh Fabric .....	38
3.3 Reinforcement of Pattern Embedded Composite.....	41
3.4 Patterning on Elastomer .....	44
 <b>Chapter 4 Robot Platform Design .....</b>	 <b>46</b>
4.1 Wheel Deformation Mechanism .....	46
4.1.1 Multi-Shaft Mechanism.....	46
4.1.2 Flexible-Shaft Mechanism.....	48
4.2 Electronics and Interface.....	52
4.3 Robot Fabrication.....	53
 <b>Chapter 5 Experiment and Result.....</b>	 <b>56</b>
5.1 Wheel Characteristic .....	56
5.2 Robot Performance .....	65
 <b>Chapter 6 Conclusion.....</b>	 <b>67</b>
 Bibliography .....	 71
 국문 초록 .....	 77

## List of Tables

Table 2.1	Variables determining wheel configuration .....	28
Table 2.2	Constraints determining wheel configuration.....	29

## List of Figures

Figure 2.1	The robot with the Compliant wheel (Left) and three types of movement of the robot (Right): (a) wheel in driving movement, at high speed on flat ground, (b) caterpillar-like movement, passing through a narrow gap by means of SMA actuation, (c) legged-wheel motion, climbing a stair by means of SMA and motor actuation.. .....	7
Figure 2.2	Eight rigid segments on a wheel and pairs of SMA coil spring actuators attached to each segment for deformation. (a) A total of sixteen actuators are attached to one wheel. The left and the right side of the wheel have four pairs of actuators, respectively. (b) Actuating two pairs at both the left and the right side induces wheel deformation.. .....	7

Figure 2.3	Unfolded and folded shape of space sail membrane. Body of wheel is made by paper and manually folded. Edge of wheel reinforced by CFRP. ....	9
Figure 2.4	Schematic of shape transformation mechanism (Left) and the robot prototype using the proposed diameter variable wheel (Right).....	9
Figure 2.5	Spherical waterbomb tessellated pattern. The shape changes from a prolate spheroid (a) to an oblate spheroid (b) in response to external force. ....	11
Figure 2.6	Unit pattern (a) and folded shape (b) of the waterbomb pattern. The blue line signifies a valley fold, and the red line signifies a mountain fold.....	11
Figure 2.7	Pattern of the origami wheel structure. A blue line signifies a valley fold, and a red line signifies a mountain fold (a). Final folded waterbomb shape (b).....	12
Figure 2.8	Waterbomb folding pattern with added bridge components at its top and bottom (a). Folded shape of the modified pattern (b). .	13
Figure 2.9	Hub component design for the wheel structure .....	13
Figure 2.10	Final shape and the components of the variable-diameter wheel.....	14



Figure 2.11	Graphical view of symbol rules for structure analysis. Because of its symmetry, the entire structure can be represented by the position of a point on two lines..	15
Figure 2.12	Design parameters for the wheel. Three length parameters determine the wheel design because the number of patterns is specified.	16
Figure 2.13	Coordinates, points, and variables for representing the wheel hub. The configuration of the wheel hub is determined by variables $\theta_{\mathcal{H}1}$ and $\theta_{\mathcal{H}2}$	16
Figure 2.14	Symmetry condition line of the wheel hub.	18
Figure 2.15	Coordinates, points, and variables for representing the wheel support. The configuration of the wheel support is determined by variables $\theta_{\mathcal{S}1}$ , $\theta_{\mathcal{S}2}$ , $\theta_{\mathcal{S}3}$ , and $\theta_{\mathcal{S}4}$ .	19
Figure 2.16	Geometrical constraint of the wheel support.	19
Figure 2.17	Symmetry condition line of the wheel support.	21
Figure 2.18	Coordinates, points, and variables for representing the wheel rim. The configuration of the wheel rim is determined by variables $\theta_{\mathcal{R}1}$ and $\theta_{\mathcal{R}2}$ .	22
Figure 2.19	General coordinate $\Sigma_{\mathcal{W}}$ for the parts assembly. The variables $\eta_{\mathcal{S}}$ and $\eta_{\mathcal{H}}$ represent the relative position of $\Sigma_{\mathcal{S}}$ , $\Sigma_{\mathcal{H}}$ in the z-direction.	24
Figure 2.20	Graphical summary of assembly points.	24

Figure 2.21	Design summary of variable-diameter wheel pattern. The patterning on the flexible material overly constrains movement, but adding flexible facets adjusts the degrees of freedom. ....	31
Figure 2.22	Schematic diagram of the minimum and maximum wheel diameters.....	32
Figure 2.23	Schematic diagram of the flexible facet. ....	33
Figure 2.24	Tendency of maximum distance to vary as length of the flexible facet increases. A value of 4.47 mm of the length of the flexible facet (about 18% of the length of the unit pattern), has been chosen. ....	34
Figure 2.25	Grouser attachment area (a) and schematic of grouser deployment (b). ....	35
Figure 2.26	Design of the wheel grouser. ....	35
Figure 3.1	Concept design of pattern enclosed composite. The facet materials are machined and enclosed by the fold line material. (a) Structure components, (b) Laminated shape, (c) Side view of result. ....	36
Figure 3.2	Fabrication procedure of pattern embedded composite. ....	37
Figure 3.3	Fabrication result of magic-ball origami pattern using various facet material: (a) Acrylic plate, (b) PET, (c) Polyimide film...	38
Figure 3.4	Wheel fabrication process using mesh fabric. ....	39
Figure 3.5	Wheel fabrication results. ....	41

Figure 3.6	Reinforcement of the laminating force by sewing.....	42
Figure 3.7	Reinforcement of the assembling force by bolting .....	43
Figure 3.8	Fabrication of elastomer (urethane) based wheel structure. ....	45
Figure 4.1	Two different methods for varying wheel diameter. ....	46
Figure 4.2	Wheel transformation mechanism using sliding shaft. ....	46
Figure 4.3	Multi shaft structure for cable twisting problem. The middle shaft decouple the sliding shaft and the torque transmission shaft....	47
Figure 4.4	Schematic of the wheel deformation mechanism using a flexible shaft. The coil spring allows the shaft to be wound up on the pulley and prevents twisting. The internal wire prevents extension of the coil spring. ....	49
Figure 4.5	Wheel hub design for the axis misalignment problem.....	50
Figure 4.6	Overall view of the wheel deformation and torque transmission mechanisms.....	51
Figure 4.7	Assembly view and components of the wheel deformation mechanism. ....	52
Figure 4.8	Control interface block diagram.....	53
Figure 4.9	3D printed robot components.....	54
Figure 4.10	Final assembled robot. ....	55
Figure 5.1	Experimental setup for the wheel diameter variation. ....	57

Figure 5.2	Experimental results of the wheel diameter variation. The graph (a) is a force-displacement profile for wheel deformation, and the graph (b) shows deformation cost. The area in graph (a) presents a $\pm 1$ standard deviation. The existence of flexible facets dramatically reduces the deformation cost and standard deviation. ....	58
Figure 5.3	Experimental setup for wheel payload. ....	60
Figure 5.4	Experimental results of the wheel payload test. The graph (a) shows the force-displacement profile for the wheel payload response, and the graph (b) shows the maximum payload with initial stiffness (in 5% linearity). As the length of the flexible facet increases, the wheel become stable and maximum payload and initial stiffness also become high, but beyond a certain length a large flexible facet cannot hold the structure, and it collapses easily. ....	61
Figure 5.5	Experimental setup for payload test at various temperature... ..	62
Figure 5.6	Experimental results of the wheel payload test at various temperature. (a) presents the result of the original specimen and (b) presents the result of the reinforced specimen. ....	63
Figure 5.7	Payload comparison at various temperature .....	64
Figure 5.8	Wheel diameter variations of the robot.. ....	65
Figure 5.9	Video snapshots of the maneuverability performance test.....	66

## Nomenclature

$l_t$	Length of the deformation trigger bar
$l_h$	Half-length of the hub plate
$l_u$	Half-length of the unit pattern
$n$	Repeated numbered of the unit pattern in circumference direction
$\Sigma_{\mathcal{W}}$	Reference frame based on the assembled wheel structure
$\Sigma_{\mathcal{H}}$	Reference frame based on the wheel hub structure
$\Sigma_{\mathcal{S}}$	Reference frame based on the wheel support structure
$\Sigma_{\mathcal{S}'}$	Reference frame based on the wheel support structure including the height
$\Sigma_{\mathcal{R}}$	Reference frame based on the wheel rim structure
$\Sigma_{\mathcal{R}'}$	Reference frame based on the wheel support structure including the height
$A_{\mathcal{H}i}$	$i^{\text{th}}$ point on line A in the wheel hub structure
$A_{\mathcal{S}i}$	$i^{\text{th}}$ point on line A in the wheel support structure
$A_{\mathcal{R}i}$	$i^{\text{th}}$ point on line A in the wheel rim structure
$\theta_{\mathcal{H}i}$	$i^{\text{th}}$ variable angle in the wheel hub structure
$\theta_{\mathcal{S}i}$	$i^{\text{th}}$ variable angle in the wheel support structure
$\theta_{\mathcal{R}i}$	$i^{\text{th}}$ variable angle in the wheel rim structure

$\eta_{\mathcal{H}}$	Relative z-position of the wheel hub reference frame from the wheel center
$\eta_{\mathcal{S}}$	Relative z-position of the wheel support reference frame from the wheel center
$\eta_{A\mathcal{SH}}$	z-position of conjunction point of the wheel support with the wheel hub in line A
$\eta_{B\mathcal{SH}}$	z-position of conjunction point of the wheel support with the wheel hub in line B
$\rho_{\mathcal{S}}$	Radius value of the wheel support reference frame from the wheel center
$\rho_{\mathcal{R}}$	Radius value of the wheel support reference frame from the wheel center
$\rho_{A\mathcal{SH}}$	Radius value of conjunction point of the wheel support with the wheel hub in line A
$\rho_{B\mathcal{SH}}$	Radius value of conjunction point of the wheel support with the wheel hub in line B
${}^{\lambda}\mathbf{x}_{\delta}$	x-value of the point $\delta$ based on the reference frame $\lambda$
${}^{\lambda}\mathbf{p}_{\delta}$	Position vector of the point $\delta$ based on the reference frame $\lambda$
${}^{\lambda}\widehat{\mathbf{p}}_{\delta}$	Position vector of the point $\delta$ based on the reference frame $\lambda$ in cylindrical coordinate

# Chapter 1 Introduction

## 1.1 Motivation

### 1.1.1 Transformable Wheel Mechanism

A mobility of mobile service robots in an unstructured environment becomes an important performance factor as the scope of applications increases from houses to disaster areas. Various terrestrial locomotion concepts have been explored, including wheels, legs, tracked locomotion, and hybrids of these concepts [1]. A leg mechanism provides agile movement in various types of terrain, but its high degrees of freedom requires a highly complex system [2-4]. A wheel mechanism allows simple and stable movement, but its mobility in rugged terrain is seriously limited.

To overcome the defects of the leg and wheel mechanisms, several characteristics of legs have been adapted to the wheel. Combining the morphological advantages of legs with a simple rotating wheel creates a rotary leg type that is much less complex [5-8]. Another important characteristic of the leg is changeable configuration. If the shape of the wheel can be made changeable, the robot will be able to pass over various types of terrain such as big obstacles and narrow gaps. Chen et al. proposed the Quattroped, a robot that can reversibly transform its wheels to legs [9], and Kim et al. proposed a wheel transformable robot with a passive rotary leg [10]. Nagatani et al. proposed a variable-diameter wheeled robot [11], and She et al. proposed a variable-diameter wheeled robot with a passive leg [12].

### **1.1.2 Soft Robotic Design Approach**

The transformable wheel mechanisms have been developed based on rigid body mechanics, but morphing characteristic of soft robot has a potential to be utilized to design of transformable wheel.

Soft robotics, a concept contrary to conventional “hard” robotics, is a robot design methodology inspired by natural. A hard robot, which is usually composed of rigid links and joints, displays a strict separation between structure and actuator. In contrast, soft robots attain infinite degrees of freedom from the soft materials of which they are made (e.g., elastomer and fabric), thereby achieving unique characteristics: dexterous motion, deformability, and adaptability to environments [13-15]. Soft robotics can also be a cheaper and simpler way to design a complex movement, and it allows for a more robust design under impact. It can also display a movement that is highly adaptable to different environments. Although soft materials involve some uncertainty and cannot offer the high strength that is offered by rigid materials in conventional robotics, their unusual characteristics are sufficient to fascinate many researchers. This design concept has been applied to mobile robots which enables various advantages. Shepherd et al. presented multigait soft robot with highly adaptive movement [16]. Loeffe et al. presented novel movement method – jumping by combustion [17], and Waynelovich et al. presented dexterous leg system using multi-chamber leg design [18].



### **1.1.3 Origami Inspired Design Approach**

Using soft materials for a variable-diameter wheel accompanies two advantages – high deformability and ability to absorb impact, but inadequate stiffness and excessive degrees of freedom can impede a wheel's functionality. The key idea is to overcome these deficiencies by making the wheel structure from a soft material to which an origami pattern has been applied, which reduces the material's excessive degrees of freedom and increases the structure's stiffness.

Origami is the art of paper folding. The innate characteristics of origami derive from its metamorphic nature; a single sheet of paper can be turned into numerous three-dimensional (3D) shapes depending on how it is folded. The unique characteristic of origami have long attracted attention from various fields such as design, education and mathematics [19-24]. Many of today's engineers are using this oriental art to solve problems [25, 26]. It can be used as an inspiration to some architectural & structural designs [27-29], and can also be used as fabrication method of robotic mechanism [30-36], medical application [37, 38] or MEMS process [39, 40].

## **1.2 Research Objectives and Contributions**

The main objective of the research is proposal of a novel variable-diameter wheel mechanism based on an origami-based soft robotics design approach. The thesis present a design and a fabrication method, and provides a comprehensive analysis of the wheel structure. Also, the thesis contains the robot design with the wheel transformation mechanism. By patterning a rigid material on a soft material, it is possible to construct a substrate with flexible regions (folding parts) that provide high deformability and rigid regions (facets)

that regulate excessive degrees of freedom and increase stiffness, for improved functionality. By using two types of facets—a rigid one and a flexible one, it is possible to adjust the wheel structure’s degrees of freedom. Instead of just distinguishing the facets and fold-lines as in a conventional origami design, our method uses facets of different stiffnesses, which can allow for high design flexibility.

Although the proposed design loses one major advantage of soft robots, high adaptability provided by a soft material’s high degrees of freedom, it provides three key advantages. First, the structure can be built without lots of mechanical parts or a complex assembly process. A single sheet replaces most parts, and a folding part generates each joint. This reduces not only the fabrication cost for each part but also the time required for assembly. Second, an origami structure can have high stiffness and impact capacity compared to its weight. In complex kinematic structures, the local distortion of links and joint alignments strongly affects how a structure moves. However, an origami structure is composed of compliant folding parts and facets, so the whole structure can perform as a shock absorber. Also, a specially organized origami structure such as a honeycomb greatly increases the effective stiffness of the whole structure. Third, an origami structure is scalable. The structure generates a joint by folding, and this reduces friction between the links. The simplified assembly process made possible by using origami structures reduces the difficulty of assembling small-scale parts.

### **1.3 Research Overview**

The thesis is arranged as follows. Design of the variable-diameter wheel section explains how the origami pattern components were designed and presents a kinematic analysis of the wheel structure with attention to the selection of design parameters. Wheel fabrication section describes fabrication of the wheel. Laser machining is used for the patterning and a mesh fabric to reinforce the adhesive force. Robot design section presents the robot's wheel deformation mechanism and its platform, which use special components such as temporarily assembled hubs and a flexible shaft. Performance evaluation section presents the performance of the wheel and the robot. The fabricated wheel structure weighs about 9.7 g and can bear more than 400 times its weight, and the robot can change the wheel diameter from 30 mm to 68 mm, allowing it to pass through a 50-mm gap and climb a 50-mm step.

## **Chapter 2. Variable-Diameter Wheel Design**

### **2.1. Origami Pattern Design for Variable-diameter Wheel**

#### **2.1.1. Rolled-up Compliant Wheel**

The compliance of the wheel gives it a high adaptability to the environment, such as being able to pass through a small gap or climb a high step. The first trial to realize this concept is using the simply rolled-up the patterned compliant structure. By combining the deformation functionality with that of a conventional wheel, a robot can move fast on a flat terrain and adapt to a more challenging environment when needed (Fig. 2.1) [41].

There are a number of critical issues involved in realizing this concept. The first is the actuation of a structure with a high degree of freedom. The compliance of the structure induces many degrees of freedom, which usually requires a large number of actuators. We propose a wheel design that uses an SMA coil spring actuator for deforming and rolling the wheel in its deformed shape (Fig. 2.2). The second critical issue regards the torque transmission as the wheel undergoes changes in its shape. Although the wheel structure can assume various shapes, to provide stable torque transmission, there must be sustainable linkage between the wheels and the drive shaft. To address that, the novel design of a spoke that can transmit the appropriate torque even as the wheel undergoes changes in its shape was proposed. The third issue, fabrication, is quite important in soft robotics. While the wheel must be sufficiently compliant to allow for easy deformation, it must also be sufficient rigid to control and maintain stiffness. To meet these two requirements, the composite that consists of segmented rigid parts and a flexible base part was designed.

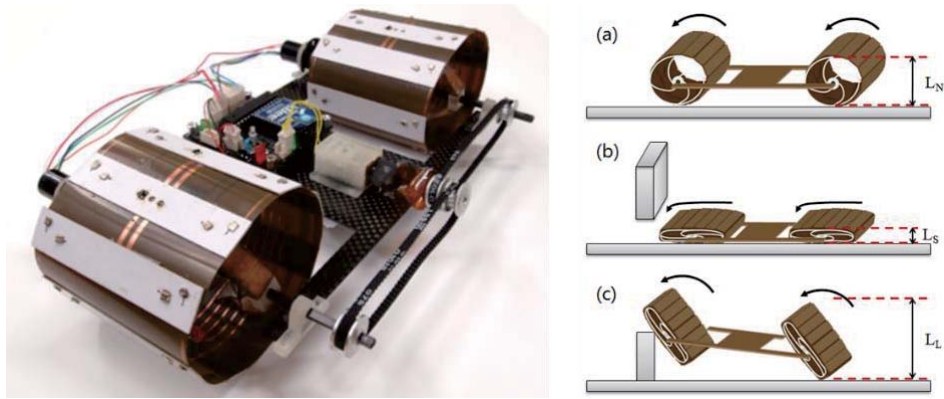


Fig. 2.1. The robot with the Compliant wheel (Left) and three types of movement of the robot (Right): (a) wheel in driving movement, at high speed on flat ground, (b) caterpillar-like movement, passing through a narrow gap by means of SMA actuation, (c) legged-wheel motion, climbing a stair by means of SMA and motor actuation.

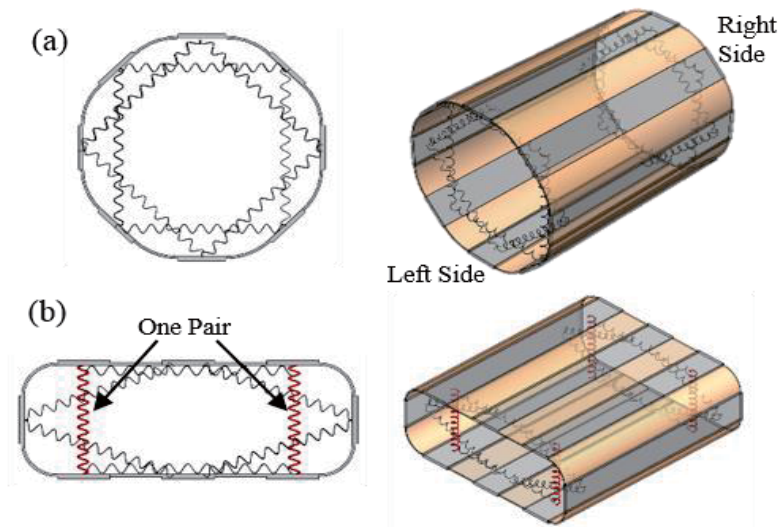


Fig. 2.2. Eight rigid segments on a wheel and pairs of SMA coil spring actuators attached to each segment for deformation. (a) A total of sixteen actuators are attached to one wheel. The left and the right side of the wheel have four pairs of actuators, respectively. (b) Actuating two pairs at both the left and the right side induces wheel deformation.

The robot provide high adaptability with the environment - the wheel radius of robot is 25 mm but it can pass 30 mm gap and climb 45mm step. However a high degree of freedom of the structure requires many actuators to provide the needed degree of control. In this robot, a series of SMA actuators was used to control the structure. This design not only cause a control problem, but also energy consumption and system robustness problem.

### **2.1.2. Spiral Foldable Pattern**

To solve the problem of previous version, the origami structure was chosen which always maintain circular shape while the diameter is varied. This means that the structure should have restricted degrees of freedom, thereby it constraint the unnecessary deformation without diameter changing. The origami model proposed by S. D. Guest et al, which was originally developed for folding inextensible space sail membrane [42] can accomplish this functionality (Fig. 2.3).

This structure has two main advantages. First is the shape. All the segments of the wheel are linked together and enable the structure to maintain a circular shape independent of whether it is folded or not. This is one of the main reasons why this structure is selected to be used as a wheel.

Second is the force transmissibility and the stiffness maintenance. A wheel that supports the whole body of the robot usually encounters a stiffness problem. How much weight the wheels can endure is main issue of the wheel, and it is even more important for deformable wheel which usually has flexible structure for deformation. Since whole wheel structure is linked together in this wheel, controlling the stiffness of every segment is not required. Stiffness of the wheel can be controlled easily by controlling a certain portion of the structure. This

property also reduces the number of actuators. It means that actuator is not needed in every segment for controlling whole system. This reduces complexity of the system and increase power efficiency in shape changing.

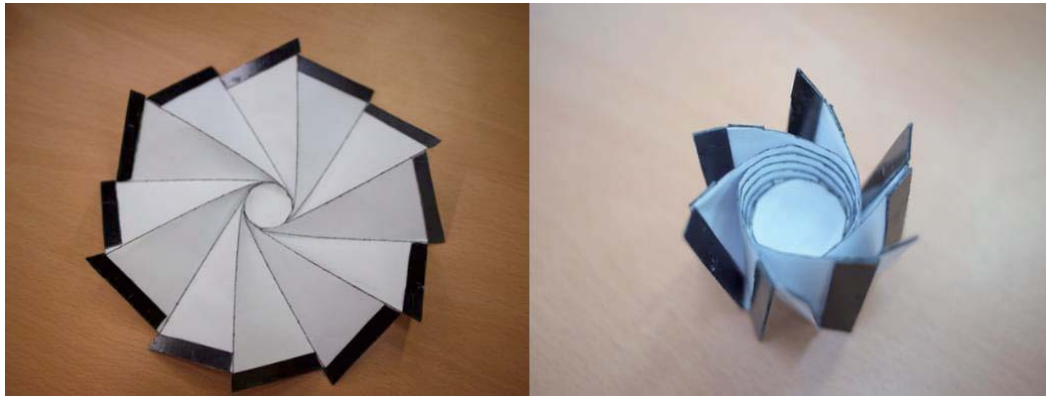


Fig. 2.3. Unfolded and folded shape of space sail membrane. Body of wheel is made by paper and manually folded. Edge of wheel reinforced by CFRP

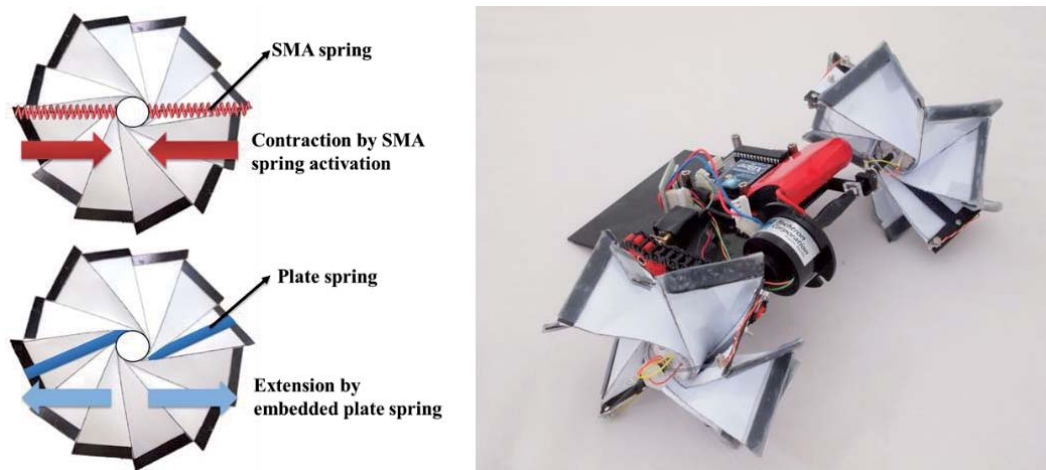


Fig. 2.4. Schematic of shape transformation mechanism (Left) and the robot prototype using the proposed diameter variable wheel (Right).

The proposed pattern is used in the previous version of the variable diameter wheel robot (Fig. 2.4) [43]. The wheel is built using a paper that is reinforced with a carbon fiber at the edges and two plate springs are embedded in the wheel to maintain stiffness and recover from contraction. Four SMA spring actuators are installed for contraction. The diameter of the wheel is 11cm in normal state and reduces to 4 cm, when contracted. This transformable wheel concept can be used to build mobile robots that can move quickly with large wheels and also move through small gaps when required.

However, the proposed structure has parallel force direction in payload and transformation. This cause a problem that the actuation force should be proportional to payload which make it difficult to increase the payload force. Waterbomb tessellation pattern is proposed to solve this problem in the next section.

### **2.1.3. Modified Waterbomb Tessellation Pattern**

The unique characteristic of the spherical waterbomb tessellated pattern can be utilized for the variable-diameter wheel structure. This structure has been used in several other applications because of its unique characteristic [35-37]. The entire shape of the waterbomb structure can be made to change from a prolate spheroid to an oblate spheroid, and therefore the structure's variable circular circumference can be used as a diameter-changing mechanism (Fig. 2.5).



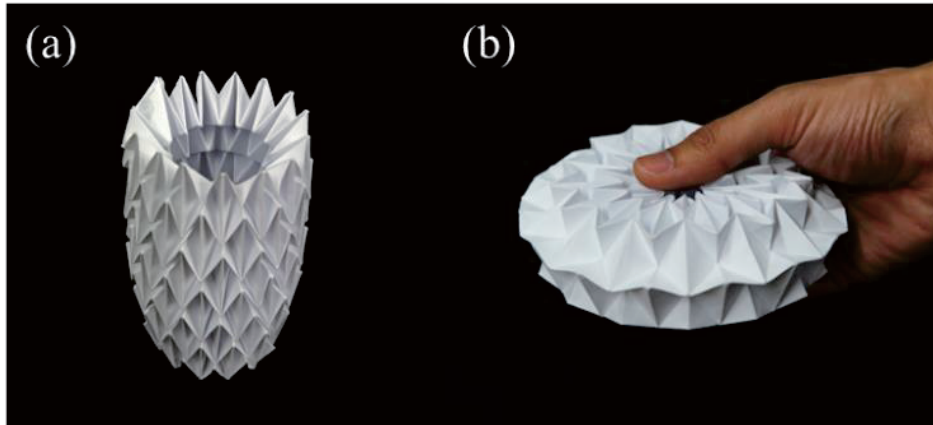


Fig. 2.5. Spherical waterbomb tessellated pattern. The shape changes from a prolate spheroid (a) to an oblate spheroid (b) in response to external force.

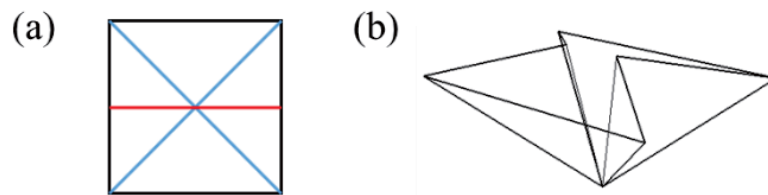


Fig. 2.6. Unit pattern (a) and folded shape (b) of the waterbomb pattern. The blue line signifies a valley fold, and the red line signifies a mountain fold.

The entire structure is composed of the waterbomb unit pattern. Eight units are repeated in a circumferential direction to make a circular rim shape, and three units are repeated in the axial direction to make the support structure (Fig. 2.7).

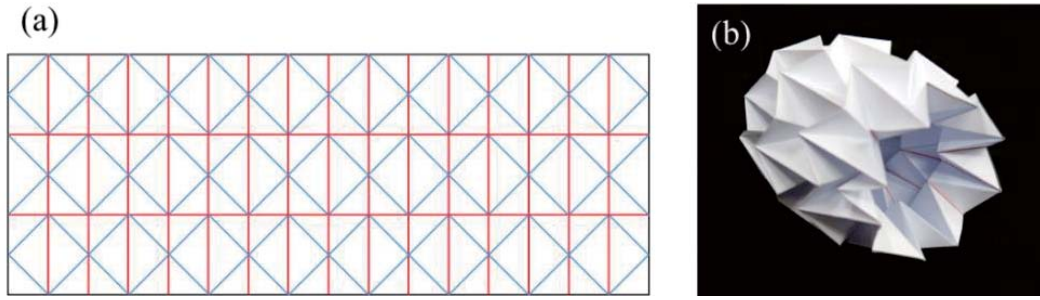


Fig. 2.7. Pattern of the origami wheel. (a) A blue line signifies a valley fold, and a red line signifies a mountain fold. (b) Final folded waterbomb shape.

The design of the connection between the wheel and the wheel shaft is important for stable movement and torque transmission. Movement of the wheel structure causes complex shape changes at its ends. However, these ends need to maintain a specific configuration to permit the wheel structure to be connected to a shaft. To solve this problem, a bridging pattern was added to the beginning and end of the waterbomb folding pattern to create a new shape at both ends of the folded structure, as shown in Fig. 2.8. The bridge design allows the ends of the modified wheel structure to remain perpendicular to the shaft and to maintain their configuration even when the wheel shape is deformed, so that the ends can work as joints and connect the wheel to a hub component. Fig. 2.9 shows a hub component that is compatible with the ends of the modified wheel structure.

The final shape of the wheel is shown in Fig. 2.10. The wheel structure has three parts. The wheel hub part makes a connection between the wheel shaft and the wheel, maintaining the wheel in a circular shape. The wheel support part can vary the wheel's diameter by changes in its slope angle. The wheel rim part forms the main body of the wheel, and it can be extended or shrunk to vary the wheel's diameter.

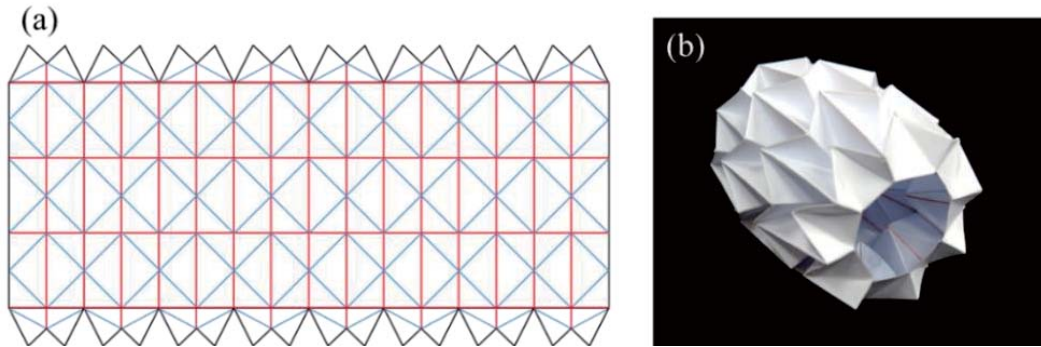


Fig. 2.8. Waterbomb folding pattern with added bridge components at its top and bottom (a). Folded shape of the modified pattern (b).

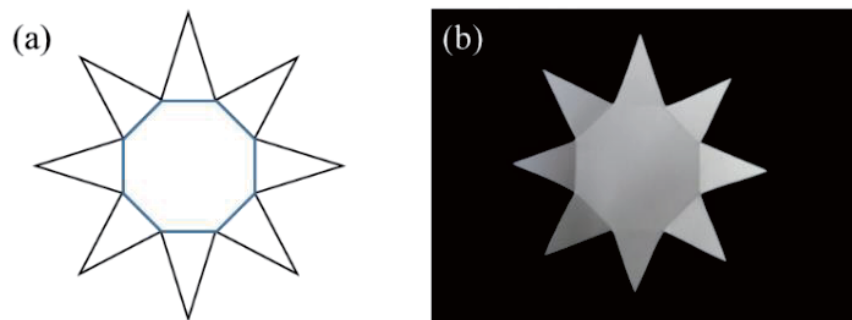


Fig. 2.9. Hub component design for the wheel structure.

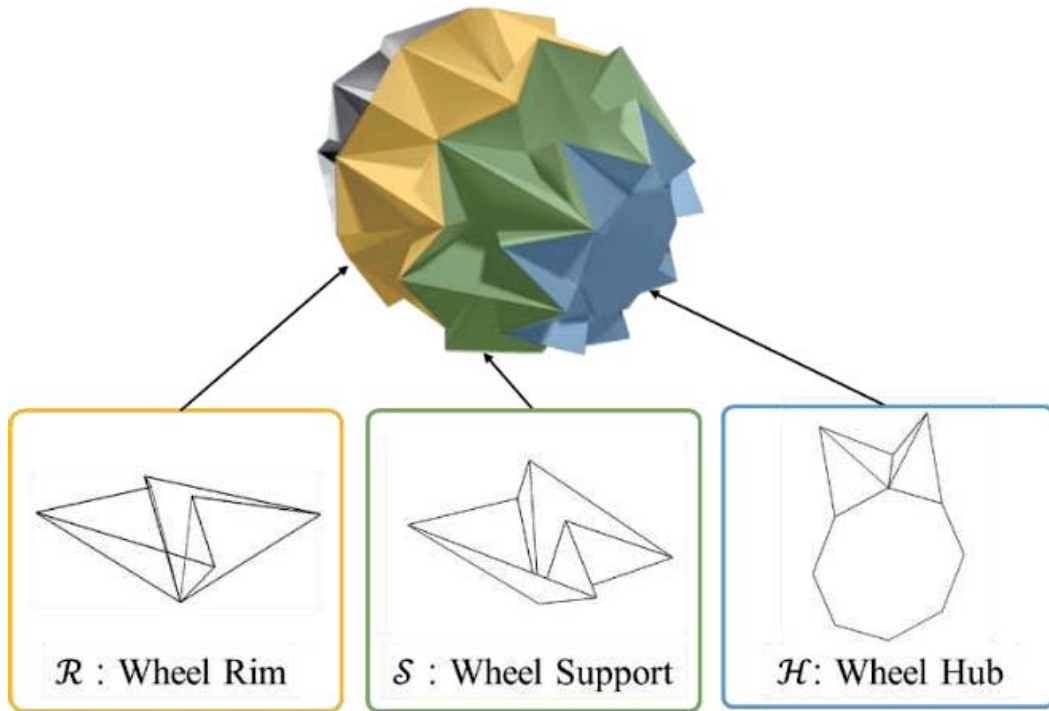


Fig. 2.10. Final shape and the components of the variable-diameter wheel.

## 2.2. Structure Analysis and Improvement

### 2.2.1. Kinematic Analysis

Technically, the origami structure cannot follow ideal rigid body kinematics. A fold line cannot be an ideal line and should have a specific width. Also, facets may bend owing to compliance of the material from which the structure is made. In other words, the structure can move regardless of its kinematic mobility. Although the kinematics of the structure cannot perfectly constrain the structure, kinematic analysis is still important because kinematics determines the moving direction of the structure, and lack of kinematic mobility hinders movement. To ensure mobility and improve deformation performance, kinematic analysis of the wheel structure was conducted based on the assumption that the folding part is an ideal revolute joint.

The wheel structure analysis was conducted in three steps. First, we specified the variables and derived the constraints from the geometry of each part. These variables and constraint equations determine the configuration of each part. Next, the symmetry constraints for maintaining the circular shape of the wheel were added. In last step, the constraints for assembling of each part were derived.

The symbol rules for points and vectors on the structure are shown in Fig. 2.11. Because it has circular symmetry, the entire structure can be represented by the position of a point on two lines, which we named line A and line B. A subscript indicates the position of points and their order.

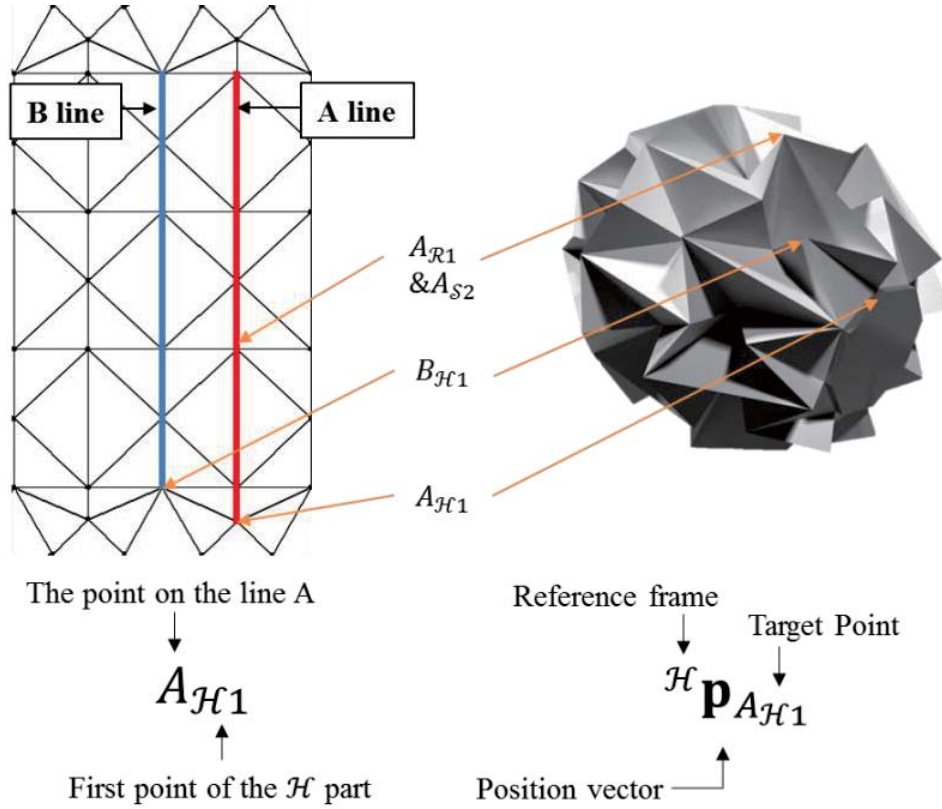


Fig. 2.11. Graphical view of symbol rules for structure analysis. Because of its symmetry, the entire structure can be represented by the position of a point on two lines.

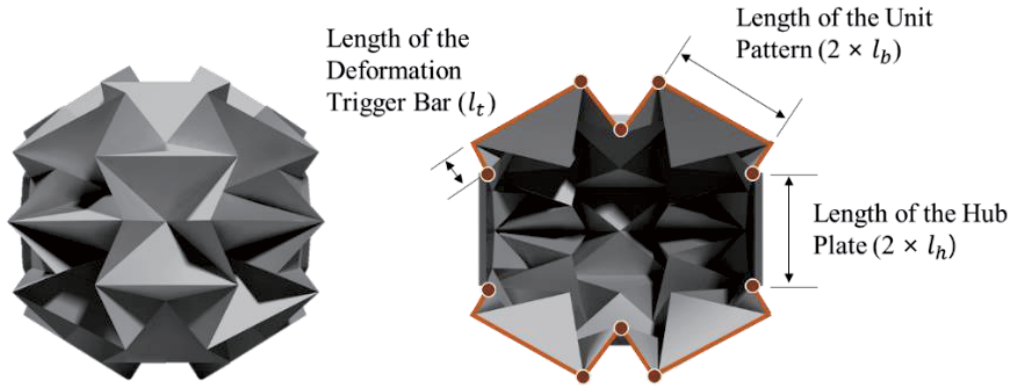


Fig. 2.12. Design parameters for the wheel. Three length parameters determine the wheel design because the number of patterns is specified.

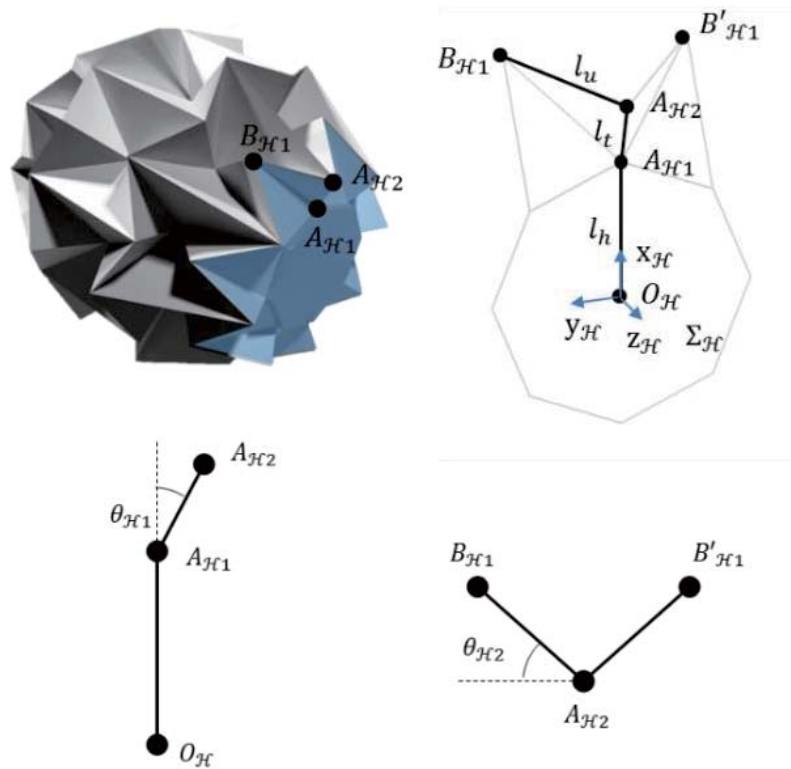


Fig. 2.13. Coordinates, points, and variables for representing the wheel hub. The configuration of the wheel hub is determined by variables  $\theta_{H1}$  and  $\theta_{H2}$ .

Because the number of patterns is specified, only three length parameters of the wheel remain (Fig. 2.12):  $l_h$ , the half-length of the hub plate;  $l_t$ , the length of the deformation trigger bar, and  $l_u$ , the half-length of the unit pattern. Fig. 2.13 shows the coordinates, points, and variables for representing the wheel hub. The reference frame  $\Sigma_{\mathcal{H}}: o_{\mathcal{H}} - x_{\mathcal{H}}y_{\mathcal{H}}z_{\mathcal{H}}$  is used to present the position vector for the points on the wheel hub. The configuration of the wheel hub is determined by two variables,  $\theta_{\mathcal{H}1}$  and  $\theta_{\mathcal{H}2}$ . From the defined parameters, the position vectors of the points of the wheel hub can be derived as follows:

$${}^{\mathcal{H}}\mathbf{p}_{A_{\mathcal{H}1}} = \begin{bmatrix} l_h \\ 0 \\ 0 \end{bmatrix} \quad (1)$$

$${}^{\mathcal{H}}\mathbf{p}_{A_{\mathcal{H}2}} = \begin{bmatrix} l_t \cos \theta_{\mathcal{H}1} + l_h \\ 0 \\ l_t \sin \theta_{\mathcal{H}1} \end{bmatrix} \quad (2)$$

$${}^{\mathcal{H}}\mathbf{p}_{B_{\mathcal{H}1}} = \begin{bmatrix} l_t \cos \theta_{\mathcal{H}1} + l_u \sin \theta_{\mathcal{H}1} \sin \theta_{\mathcal{H}2} + l_h \\ l_u \cos \theta_{\mathcal{H}2} \\ l_t \sin \theta_{\mathcal{H}1} - l_u \cos \theta_{\mathcal{H}1} \sin \theta_{\mathcal{H}2} \end{bmatrix} \quad (3)$$

To satisfy wheel symmetry, point  $B_{\mathcal{H}1}$  should be on the symmetry condition line (Fig. 2.14). The wheel has eight repeated unit patterns in the circumferential direction, so the slope angle should be  $\frac{\pi}{8}$ , but in the equation, we keep it as  $n$  for generality. From the symmetry condition, a constraint equation is derived as follows:

$$\frac{{}^{\mathcal{H}}y_{B_{\mathcal{H}1}}}{{}^{\mathcal{H}}x_{B_{\mathcal{H}1}}} = \tan \frac{\pi}{n} = \frac{l_u \cos \theta_{\mathcal{H}2}}{l_t \cos \theta_{\mathcal{H}1} + l_u \sin \theta_{\mathcal{H}1} \sin \theta_{\mathcal{H}2} + l_h} \quad (4)$$

$$\text{Const. \#1} \quad \tan \frac{\pi}{n} \left( \frac{l_t \cos \theta_{\mathcal{H}1} + l_h}{l_u} + \sin \theta_{\mathcal{H}1} \sin \theta_{\mathcal{H}2} \right) - \cos \theta_{\mathcal{H}2} = 0 \quad (5)$$

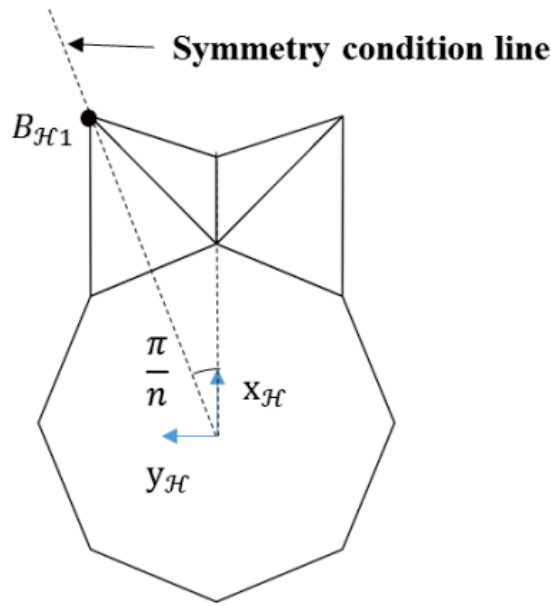


Fig. 2.14. Symmetry condition line of the wheel hub.

The analysis of the wheel support is conducted similarly to the wheel hub analysis. The reference frame  $\Sigma_{\mathcal{S}}: o_{\mathcal{S}} - x_{\mathcal{S}}y_{\mathcal{S}}z_{\mathcal{S}}$  is used to present the position vectors of the points on the wheel support. Fig. shows the coordinates, points, and variables for representing the wheel support.

The wheel support has a geometrical constraint because the length of the line  $\overline{A_{\mathcal{S}1}A_{\mathcal{S}2}}$  should have a certain value, as shown in Fig. 2.16. Equation 6 shows the condition:



$$\| {}^{\mathcal{S}}\mathbf{p}_{A_{S1}} - {}^{\mathcal{S}}\mathbf{p}_{A_{S2}} \| = 2l_u \quad (6)$$

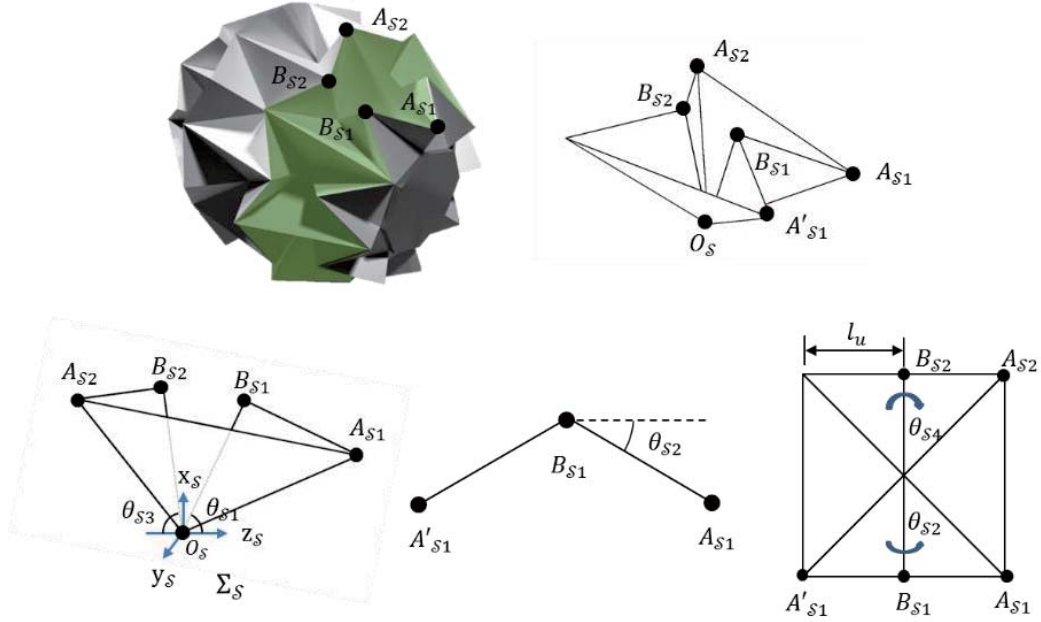


Fig. 2.15. Coordinates, points, and variables for representing the wheel support. The configuration of the wheel support is determined by variables  $\theta_{S1}$ ,  $\theta_{S2}$ ,  $\theta_{S3}$ , and  $\theta_{S4}$ .

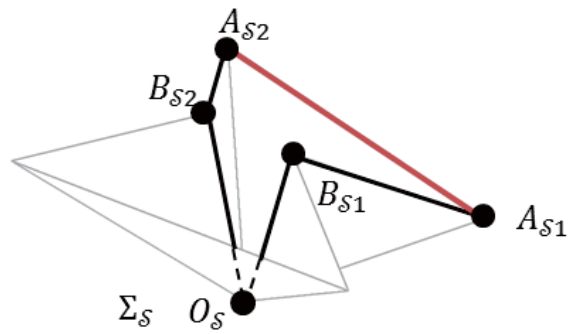


Fig. 2.16. Geometrical constraint of the wheel support.

From the position vector:

$${}^S \mathbf{p}_{A_{S1}} = \begin{bmatrix} l_u (\sin \theta_{S1} - \cos \theta_{S1} \sin \theta_{S2}) \\ -l_u \cos \theta_{S2} \\ l_u (\cos \theta_{S1} + \sin \theta_{S1} \sin \theta_{S2}) \end{bmatrix} \quad (7)$$

$${}^S \mathbf{p}_{A_{S2}} = \begin{bmatrix} l_u (\sin \theta_{S3} - \cos \theta_{S3} \sin \theta_{S4}) \\ -l_u \cos \theta_{S4} \\ -l_u (\cos \theta_{S3} + \sin \theta_{S3} \sin \theta_{S4}) \end{bmatrix} \quad (8)$$

The constraint equation is derived as

$$\begin{aligned} \textbf{Const. \#2: } & (\sin \theta_{S2} + \sin \theta_{S4}) \sin(\theta_{S1} + \theta_{S3}) \\ & + (1 - \sin \theta_{S2} \sin \theta_{S4}) \cos(\theta_{S1} + \theta_{S3}) - \cos \theta_{S2} \cos \theta_{S4} = 0 \end{aligned} \quad (9)$$

Similar to the wheel hub, the wheel support needs to satisfy the symmetry condition. Fig. 2.17 graphically shows the constraint. The height variable  $\rho_S$  is added to represent the height of the wheel support reference frame from the wheel center, and new reference frame  $\Sigma_{S'}$  is defined.

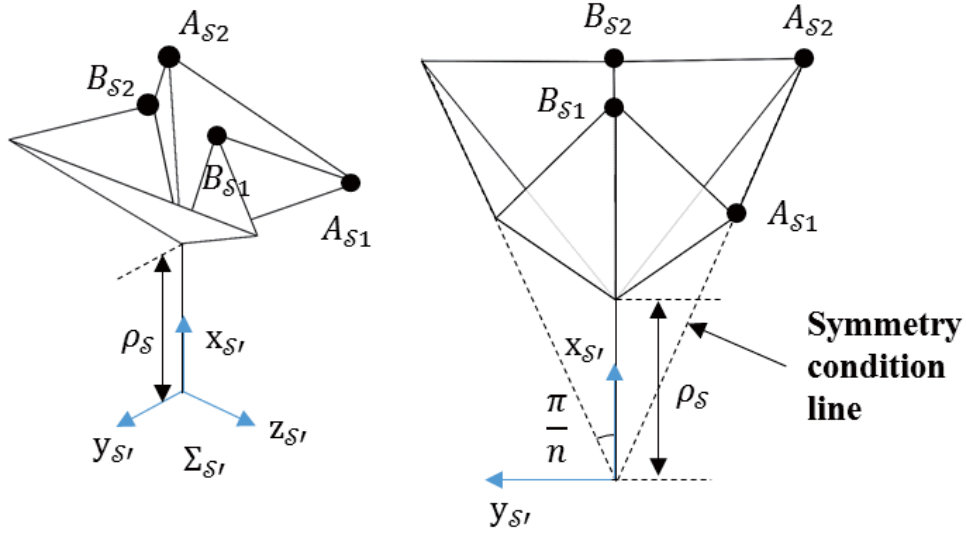


Fig. 2.17. Symmetry condition line of the wheel support.

Points  $A_{S1}$  and  $A_{S2}$  should be on the symmetry condition line so that their position vector satisfies the conditions.

$${}^{s'}\mathbf{p}_{A_{S1}} = \begin{bmatrix} \rho_S + l_u(\sin \theta_{S1} - \cos \theta_{S1} \sin \theta_{S2}) \\ -l_u \cos \theta_{S2} \\ l_u(\cos \theta_{S1} + \sin \theta_{S1} \sin \theta_{S2}) \end{bmatrix} \quad (10)$$

$${}^{s'}\mathbf{p}_{A_{S2}} = \begin{bmatrix} \rho_S + l_u(\sin \theta_{S3} - \cos \theta_{S3} \sin \theta_{S4}) \\ -l_u \cos \theta_{S4} \\ -l_u(\cos \theta_{S3} + \sin \theta_{S3} \sin \theta_{S4}) \end{bmatrix} \quad (11)$$

$$\mathbf{Const. \#3:} (\rho_S + l_u(\sin \theta_{S1} - \cos \theta_{S1} \sin \theta_{S2})) \tan \frac{\pi}{n} - l_u \cos \theta_{S2} = 0 \quad (12)$$

$$\mathbf{Const. \#4:} (\rho_S + l_u(\sin \theta_{S3} - \cos \theta_{S3} \sin \theta_{S4})) \tan \frac{\pi}{n} - l_u \cos \theta_{S4} = 0 \quad (13)$$

The geometry of the wheel rim is similar to that of the wheel support, but it has symmetry in the  $z_{\mathcal{R}}$  direction. Only two variables,  $\theta_{\mathcal{R}1}$ ,  $\theta_{\mathcal{R}2}$ , are required to determine the configuration of the part. The reference frame  $\Sigma_{\mathcal{R}}: o_{\mathcal{R}} - x_{\mathcal{R}}y_{\mathcal{R}}z_{\mathcal{R}}$  and the variables  $\theta_{\mathcal{R}1}$ ,  $\theta_{\mathcal{R}2}$  of the wheel rim are graphically presented in Fig. 2.18.

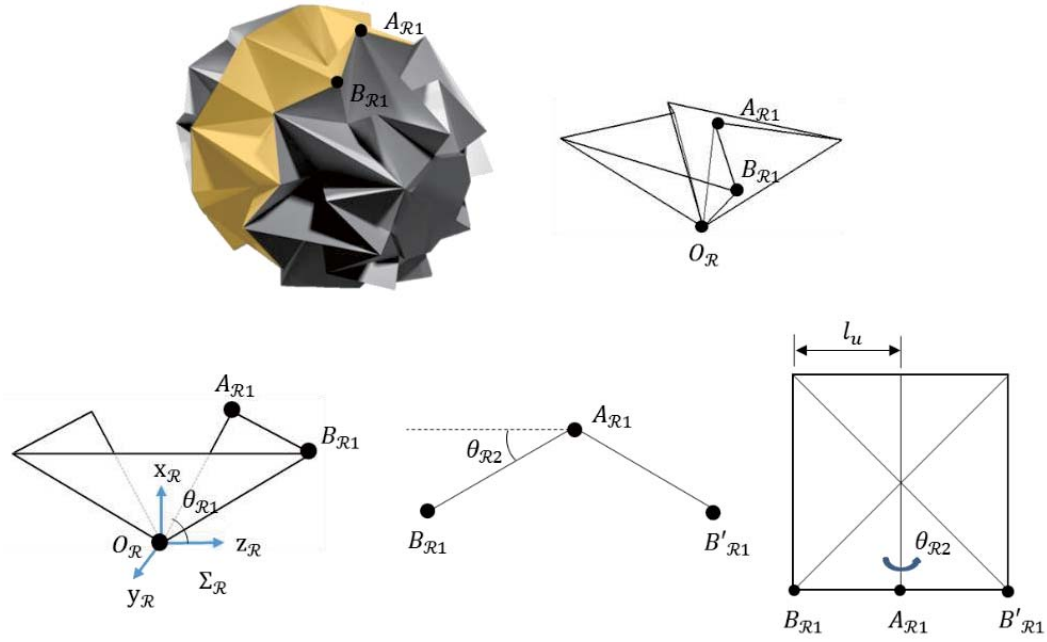


Fig. 2.18. Coordinates, points, and variables for representing the wheel rim. The configuration of the wheel rim is determined by variables  $\theta_{\mathcal{R}1}$  and  $\theta_{\mathcal{R}2}$ .

From the geometrical constraint, the  $z$  position of point  $B_{\mathcal{R}1}$  should equal  $l_u$ . The vector presentation of point  $B_{\mathcal{R}1}$  is

$${}^{\mathcal{R}}\mathbf{p}_{B_{\mathcal{R}1}} = \begin{bmatrix} l_u(\sin \theta_{\mathcal{R}1} - \cos \theta_{\mathcal{R}1} \sin \theta_{\mathcal{R}2}) \\ l_u \cos \theta_{\mathcal{R}2} \\ l_u(\cos \theta_{\mathcal{R}1} + \sin \theta_{\mathcal{R}1} \sin \theta_{\mathcal{R}2}) \end{bmatrix} \quad (14)$$

Therefore the constraint is

$$\text{Const. \#5 } (\cos \theta_{\mathcal{R}1} + \sin \theta_{\mathcal{R}1} \sin \theta_{\mathcal{R}2}) = 1 \quad (15)$$

Similar to the wheel support, the height variable  $\rho_{\mathcal{R}}$  and new reference frame  $\Sigma_{\mathcal{R}'}$  are introduced to make the symmetry condition. Because point  $B_{\mathcal{R}1}$  should be on the symmetry line as the wheel hub and the wheel support, the constraint equation can be derived from the position vector:

$${}^{\mathcal{R}'}\mathbf{p}_{B_{\mathcal{R}1}} = \begin{bmatrix} \rho_{\mathcal{R}} + l_u(\sin \theta_{\mathcal{R}1} - \cos \theta_{\mathcal{R}1} \sin \theta_{\mathcal{R}2}) \\ l_u \cos \theta_{\mathcal{R}2} \\ l_u(\cos \theta_{\mathcal{R}1} + \sin \theta_{\mathcal{R}1} \sin \theta_{\mathcal{R}2}) \end{bmatrix} \quad (16)$$

$$\begin{aligned} \text{Const. \#6 } \{ \rho_{\mathcal{R}} + l_u(\sin \theta_{\mathcal{R}1} - \cos \theta_{\mathcal{R}1} \sin \theta_{\mathcal{R}2}) \} \tan \frac{\pi}{n} - \\ l_u \cos \theta_{\mathcal{R}2} = 0 \end{aligned} \quad (17)$$

Because the three parts are assembled, new constraint equations should be derived from the assembly. To assemble all parts, a general coordinate named “wheel frame,”  $\Sigma_{\mathcal{W}}$ , is introduced as shown in Fig. 2.19. New variables  $\eta_{\mathcal{S}}$ ,  $\eta_{\mathcal{H}}$ , representing the relative position of  $\Sigma_{\mathcal{S}}$ ,  $\Sigma_{\mathcal{H}}$  in the z-direction, are used. For convenience, all coordinates are presented in cylindrical form, and the symbol  $\hat{\mathbf{p}}$  is used to indicate the point vector in a cylindrical coordinate.

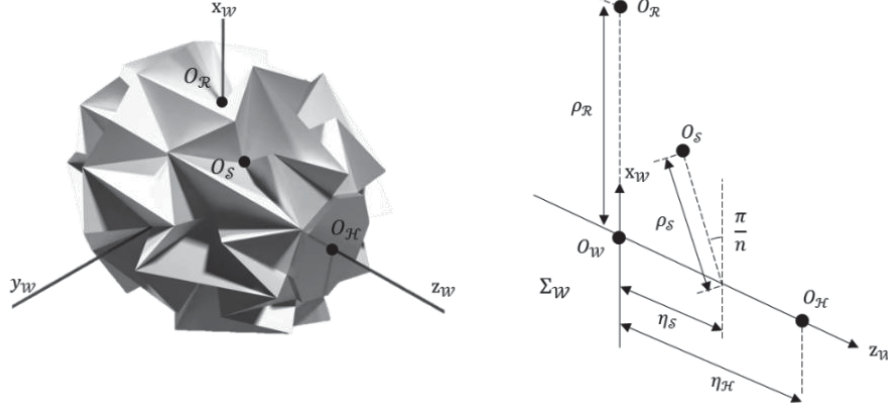


Fig. 2.19. General coordinate  $\Sigma_W$  for the parts assembly. The variables  $\eta_S$  and  $\eta_H$  represent the relative position of  $\Sigma_S$ ,  $\Sigma_H$  in the z-direction.

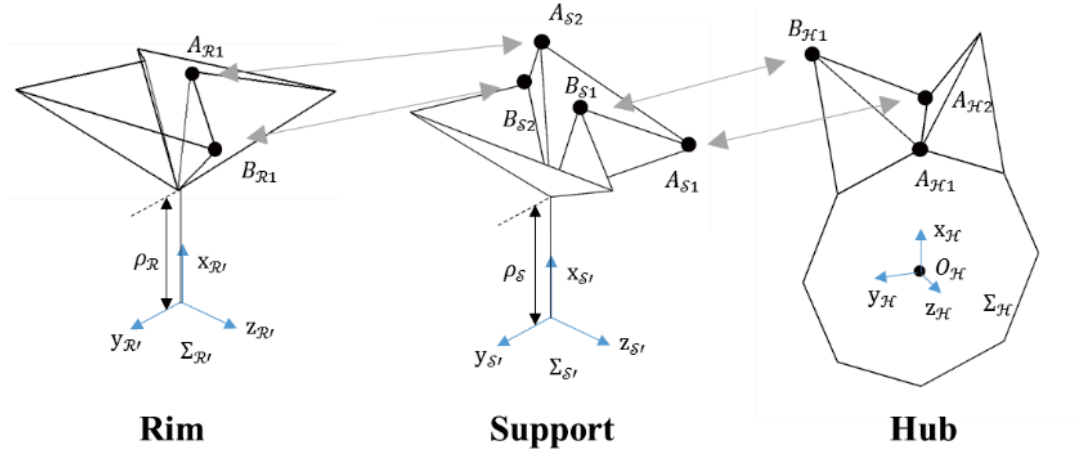


Fig. 2.20. Graphical summary of assembly points.

To assemble the wheel support and the wheel hub, point  $A_{S1}$  on the wheel support should be at the same position as point  $A_{H2}$  on the hub. Also, points  $B_{S1}$  and  $B_{H1}$  should be at the same positions. Similarly, points  $A_{R1} - A_{S2}$  and  $B_{R1} - B_{S2}$  should be at the same positions for assembly of the wheel rim and the wheel support (Fig. 2.20).

The position vectors of  $A_{S1}$  and  $A_{H2}$  in the cylindrical coordinate are presented as

$${}^w\widehat{\mathbf{p}}_{A_{S1}} = \begin{bmatrix} l_u \cos \theta_{S2} / \sin \frac{\pi}{n} \\ 0 \\ \eta_S + l_u \cos \theta_{S1} + l_u \sin \theta_{S1} \sin \theta_{S2} \end{bmatrix} \quad (18)$$

$${}^w\widehat{\mathbf{p}}_{A_{H2}} = \begin{bmatrix} l_h + l_t \cos \theta_{H1} \\ 0 \\ \eta_H + l_t \sin \theta_{H1} \end{bmatrix} \quad (19)$$

So the derived constraint equations are

$$\rho_{A_{SH}} = l_u \cos \theta_{S2} / \sin \frac{\pi}{n} = l_h + l_t \cos \theta_{H1} \quad (20)$$

$$\eta_{A_{SH}} = \eta_S + l_u \cos \theta_{S1} + l_u \sin \theta_{S1} \sin \theta_{S2} = \eta_H + l_t \sin \theta_{H1} \quad (21)$$

where  $A_{SH}$  is the assembly point in line A of the wheel support and the wheel hub. Similarly, the position vectors  $B_{S1}$  and  $B_{H1}$  in the cylindrical coordinate are presented as

$${}^w\widehat{\mathbf{p}}_{B_{S1}} = \begin{bmatrix} \rho_S + l_u \sin \theta_{S1} \\ \pi/n \\ \eta_S + l_u \cos \theta_{S1} \end{bmatrix} \quad (22)$$

$${}^w\widehat{\mathbf{p}}_{B_{H1}} = \begin{bmatrix} l_u \cos \theta_{H2} / \sin \frac{\pi}{n} \\ \pi/n \\ \eta_H + l_t \sin \theta_{H1} - l_u \sin \theta_{H2} \cos \theta_{H1} \end{bmatrix} \quad (23)$$

So the derived constraint equations are

$$\rho_{B_{\mathcal{SH}}} = \rho_{\mathcal{S}} + l_u \sin \theta_{\mathcal{S}1} = l_u \cos \theta_{\mathcal{H}2} / \sin \frac{\pi}{n} \quad (24)$$

$$\eta_{B_{\mathcal{SH}}} = \eta_{\mathcal{S}} + l_u \cos \theta_{\mathcal{S}1} = \eta_{\mathcal{H}} + l_t \sin \theta_{\mathcal{H}1} - l_u \sin \theta_{\mathcal{H}2} \cos \theta_{\mathcal{H}1} \quad (25)$$

The length between points  $A_{\mathcal{H}2}$  and  $B_{\mathcal{H}1}$  and the length between points  $A_{\mathcal{S}1}$  and  $B_{\mathcal{S}1}$  should be equal, so there is redundancy in the constraint equations. From this condition, equation (26) with equation (5) and (12) can be summarized as equation (27).

$$\eta_{A_{\mathcal{SH}}} - \eta_{B_{\mathcal{SH}}} = l_u \cos \theta_{\mathcal{H}1} \sin \theta_{\mathcal{H}2} = l_u \sin \theta_{\mathcal{S}1} \sin \theta_{\mathcal{S}2} \quad (26)$$

$$\eta_{A_{\mathcal{SH}}} - \eta_{B_{\mathcal{SH}}} = \sqrt{l_u^2 - \rho_{A_{\mathcal{SH}}}^2 - \rho_{B_{\mathcal{SH}}}^2 + 2\rho_{A_{\mathcal{SH}}}\rho_{B_{\mathcal{SH}}} \cos \frac{\pi}{n}} \quad (27)$$

The equations show that the value of  $\eta_{A_{\mathcal{SH}}} - \eta_{B_{\mathcal{SH}}}$  can be determined by the values of  $\rho_{A_{\mathcal{SH}}}$  and  $\rho_{B_{\mathcal{SH}}}$ , which means that the constraint equations for these three values determine the other value. For example, if the constraint equation for  $\rho_{A_{\mathcal{SH}}}$ ,  $\rho_{B_{\mathcal{SH}}}$ , and  $\eta_{A_{\mathcal{SH}}}$  are satisfied, the value of  $\eta_{B_{\mathcal{SH}}}$  is consequentially constrained. Therefore, four constraint equations can be reduced to three:

$$\textbf{Const. \#7: } l_u \cos \theta_{\mathcal{S}2} / \sin \frac{\pi}{n} - l_h - l_t \cos \theta_{\mathcal{H}1} = 0 \quad (27)$$



$$\text{Const. \#8: } \eta_{\mathcal{S}} + l_u \cos \theta_{\mathcal{S}1} + l_u \sin \theta_{\mathcal{S}1} \sin \theta_{\mathcal{S}2} - (\eta_{\mathcal{H}} + l_t \sin \theta_{\mathcal{H}1}) = 0 \quad (28)$$

$$\text{Const. \#9: } \rho_{\mathcal{S}} + l_u \sin \theta_{\mathcal{S}1} - l_u \cos \theta_{\mathcal{H}2} / \sin \frac{\pi}{n} = 0 \quad (29)$$

Similarly, the point vectors and the constraint equations for points  $A_{\mathcal{R}1} - A_{\mathcal{S}2}$  and  $B_{\mathcal{R}1} - B_{\mathcal{S}2}$  can be achieved as follows:

$${}^w \hat{\mathbf{p}}_{A_{\mathcal{R}1}} = \begin{bmatrix} \rho_{\mathcal{R}} + l_u \sin \theta_{\mathcal{R}1} \\ 0 \\ l_u \cos \theta_{\mathcal{R}1} \end{bmatrix} \quad (30)$$

$${}^w \hat{\mathbf{p}}_{A_{\mathcal{S}2}} = \begin{bmatrix} l_u \cos \theta_{\mathcal{S}4} / \sin \frac{\pi}{n} \\ 0 \\ \eta_{\mathcal{S}} - l_u \cos \theta_{\mathcal{S}3} - l_u \sin \theta_{\mathcal{S}3} \sin \theta_{\mathcal{S}4} \end{bmatrix} \quad (31)$$

$${}^w \hat{\mathbf{p}}_{B_{\mathcal{R}1}} = \begin{bmatrix} l_u \cos \theta_{\mathcal{R}2} / \sin \frac{\pi}{n} \\ \pi/n \\ l_u \cos \theta_{\mathcal{R}1} + l_u \sin \theta_{\mathcal{R}1} \sin \theta_{\mathcal{R}2} \end{bmatrix} \quad (32)$$

$${}^w \hat{\mathbf{p}}_{B_{\mathcal{S}2}} = \begin{bmatrix} \rho_{\mathcal{S}} + l_u \sin \theta_{\mathcal{S}3} \\ \pi/n \\ \eta_{\mathcal{S}} - l_u \cos \theta_{\mathcal{S}3} \end{bmatrix} \quad (33)$$

$$\rho_{A_{\mathcal{R}\mathcal{S}}} = \rho_{\mathcal{R}} + l_u \sin \theta_{\mathcal{R}1} = l_u \cos \theta_{\mathcal{S}4} / \sin \frac{\pi}{n} \quad (34)$$

$$\eta_{A_{\mathcal{R}\mathcal{S}}} = l_u \cos \theta_{\mathcal{R}1} = \eta_{\mathcal{S}} - l_u \cos \theta_{\mathcal{S}3} - l_u \sin \theta_{\mathcal{S}3} \sin \theta_{\mathcal{S}4} \quad (35)$$

$$\rho_{B_{\mathcal{RS}}} = l_u \cos \theta_{\mathcal{R}2} / \sin \frac{\pi}{n} = \rho_{\mathcal{S}} + l_u \sin \theta_{\mathcal{S}3} \quad (36)$$

$$\eta_{B_{\mathcal{RS}}} = l_u \cos \theta_{\mathcal{R}1} + l_u \sin \theta_{\mathcal{R}1} \sin \theta_{\mathcal{R}2} = \eta_{\mathcal{S}} - l_u \cos \theta_{\mathcal{S}3} \quad (37)$$

$$\text{Const. \#10 } \rho_{\mathcal{R}} + l_u \sin \theta_{\mathcal{R}1} - l_u \cos \theta_{\mathcal{S}4} / \sin \frac{\pi}{n} = 0 \quad (38)$$

$$\text{Const. \#11 } l_u \cos \theta_{\mathcal{R}2} / \sin \frac{\pi}{n} - (\rho_{\mathcal{S}} + l_u \sin \theta_{\mathcal{S}3}) = 0 \quad (39)$$

$$\begin{aligned} \text{Const. \#12 } & l_u \cos \theta_{\mathcal{R}1} + l_u \sin \theta_{\mathcal{R}1} \sin \theta_{\mathcal{R}2} \\ & - (\eta_{\mathcal{S}} - l_u \cos \theta_{\mathcal{S}3}) = 0 \end{aligned} \quad (40)$$

Overall, 12 variables and 12 constraint equations were derived, and the results are summarized in Table 2.1 and Table 2.2. The mechanism composed of 12 variables with 12 constraints has zero kinematic degrees of freedom. The manufactured prototype is deformable because its facets are made of compliant material. Nevertheless, material deformation causes a high force in the movement of the structure and also causes material failure because of high stress concentration. We will discuss this issue in section 2.3.

**Table 2.1. Variables determining wheel configuration**

	Angle Variable	Position Variable
Wheel hub part	$\theta_{\mathcal{H}1}, \theta_{\mathcal{H}2}$	$\eta_{\mathcal{H}}$
Wheel support part	$\theta_{\mathcal{S}1}, \theta_{\mathcal{S}2}, \theta_{\mathcal{S}3}, \theta_{\mathcal{S}4}$	$\rho_{\mathcal{S}}, \eta_{\mathcal{S}}$
Wheel rim part	$\theta_{\mathcal{R}1}, \theta_{\mathcal{R}2}$	$\rho_{\mathcal{R}}$

**Table 2.2. Constraints determining wheel configuration**

Constraint of wheel hub part	
$\tan \frac{\pi}{n} \left( \frac{l_t \cos \theta_{\mathcal{H}1} + l_h}{l_u} + \sin \theta_{\mathcal{H}1} \sin \theta_{\mathcal{H}2} \right) - \cos \theta_{\mathcal{H}2} = 0$	(5)
Constraint of wheel support part	
$(\sin \theta_{\mathcal{S}2} + \sin \theta_{\mathcal{S}4}) \sin(\theta_{\mathcal{S}1} + \theta_{\mathcal{S}3}) + (1 - \sin \theta_{\mathcal{S}2} \sin \theta_{\mathcal{S}4}) \cos(\theta_{\mathcal{S}1} + \theta_{\mathcal{S}3}) - \cos \theta_{\mathcal{S}2} \cos \theta_{\mathcal{S}4} = 0$	(9)
$(\rho_{\mathcal{S}} + l_u(\sin \theta_{\mathcal{S}1} - \cos \theta_{\mathcal{S}1} \sin \theta_{\mathcal{S}2})) \tan \frac{\pi}{n} - l_u \cos \theta_{\mathcal{S}2} = 0$	(12)
$(\rho_{\mathcal{S}} + l_u(\sin \theta_{\mathcal{S}3} - \cos \theta_{\mathcal{S}3} \sin \theta_{\mathcal{S}4})) \tan \frac{\pi}{n} - l_u \cos \theta_{\mathcal{S}4} = 0$	(13)
Constraint of wheel rim part	
$(\cos \theta_{\mathcal{R}1} + \sin \theta_{\mathcal{R}1} \sin \theta_{\mathcal{R}2}) = 1$	(15)
$(\rho_{\mathcal{R}} + l_u(\sin \theta_{\mathcal{R}1} - \cos \theta_{\mathcal{R}1} \sin \theta_{\mathcal{R}2})) \tan \frac{\pi}{n} - l_u \cos \theta_{\mathcal{R}2} = 0$	(17)
Constraint of hub support part assembly	
$l_u \cos \theta_{\mathcal{S}2} / \sin \frac{\pi}{n} - l_h + l_t \cos \theta_{\mathcal{H}1} = 0$	(28)
$\eta_{\mathcal{S}} + l_u \cos \theta_{\mathcal{S}1} + l_u \sin \theta_{\mathcal{S}1} \sin \theta_{\mathcal{S}2} - (\eta_{\mathcal{H}} + l_t \sin \theta_{\mathcal{H}1}) = 0$	(29)
$\rho_{\mathcal{S}} + l_u \sin \theta_{\mathcal{S}1} - l_u \cos \theta_{\mathcal{H}2} / \sin \frac{\pi}{n} = 0$	(30)
Constraint of support – rim part assembly	
$\rho_{\mathcal{R}} + l_u \sin \theta_{\mathcal{R}1} - l_u \cos \theta_{\mathcal{S}4} / \sin \frac{\pi}{n} = 0$	(39)
$l_u \cos \theta_{\mathcal{R}2} / \sin \frac{\pi}{n} - (\rho_{\mathcal{S}} + l_u \sin \theta_{\mathcal{S}3}) = 0$	(40)
$l_u \cos \theta_{\mathcal{R}1} + l_u \sin \theta_{\mathcal{R}1} \sin \theta_{\mathcal{R}2} - (\eta_{\mathcal{S}} - l_u \cos \theta_{\mathcal{S}3}) = 0$	(41)

### 2.2.2 Hybrid Pattern Design

The proposed structure has an equal number of variables with constraint equations, which leads to zero mobility of the mechanism. This problem can be solved by cutting the material, but that would seriously weaken the structure's robustness. Our solution to this problem is releasing the constraints by using a flexible facet in a specific region. This is simply achieved by increasing the area of the folding part. A small width of the folding part constrains most of the movement of the adjacent facets without revolute joint motion. However, increasing the area of the folding part to a level of the facet allows for much more flexible movement so that the adjacent facets gain extra degrees of freedom. This design approach—utilizing both rigid and flexible facets—allows high design.

The target constraint to be released is the assembly constraint on point  $A_{RS}$ , which is the assembly point in line A between the wheel rim and the wheel support part. We chose to release this point because it endures high external force when the wheel contacts the ground owing to its prominent geometry.

Assembly of one point generates two constraint equations. Therefore, releasing the assembly of one point generates two extra degrees of freedom. However, this also breaks the redundancy of the equations, so that the number of the constraints for assembling the wheel rim with the wheel support become two, not one. As a result, constraint 10 (equation [41]) is eliminated, and the total degrees of freedom is changed to one by using a flexible facet. The modified origami pattern is shown in Fig. 2.21. The wheel is made of two laminated materials, one rigid and one flexible, such that variation of the pattern for the rigid parts creates a flexible facet region.

Fig. 2.21 summarizes the design flow of the variable diameter wheel. By applying a modified origami pattern to the flexible substrate that includes flexible facets, we converted a structure that would have had zero degrees of freedom into one whose degrees of freedom can be adjusted.

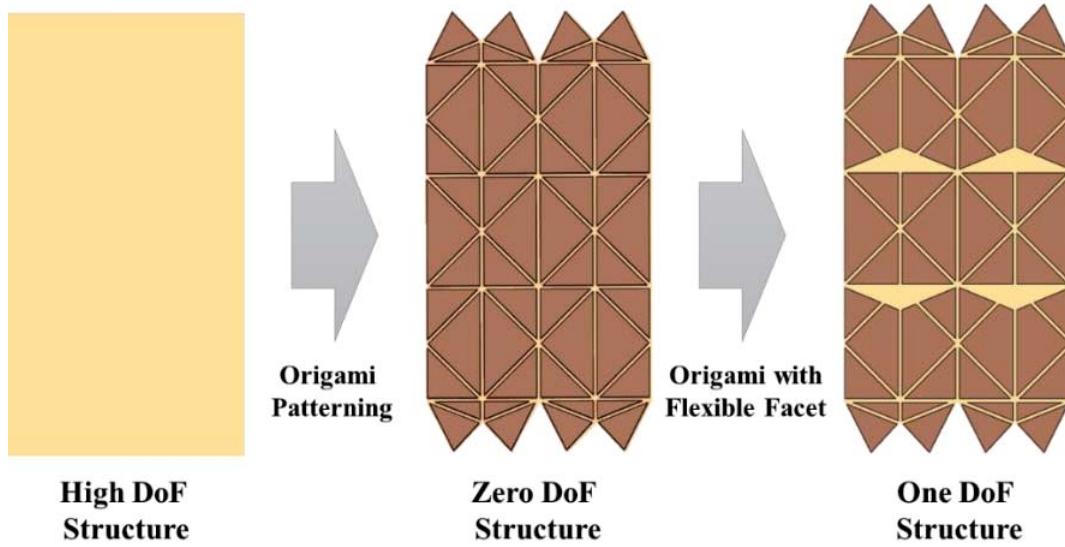


Fig. 2.21. Design summary of variable-diameter wheel pattern. The patterning on the flexible material overly constrains movement, but adding flexible facets adjusts the degrees of freedom.

### 2.2.3 Design Parameter Optimization

As discussed in previous, the wheel structure has three design parameters: length of the unit pattern, length of the hub plate, and length of the deformation trigger bar. The maximum deformation ratio can be achieved by adjusting these parameters.

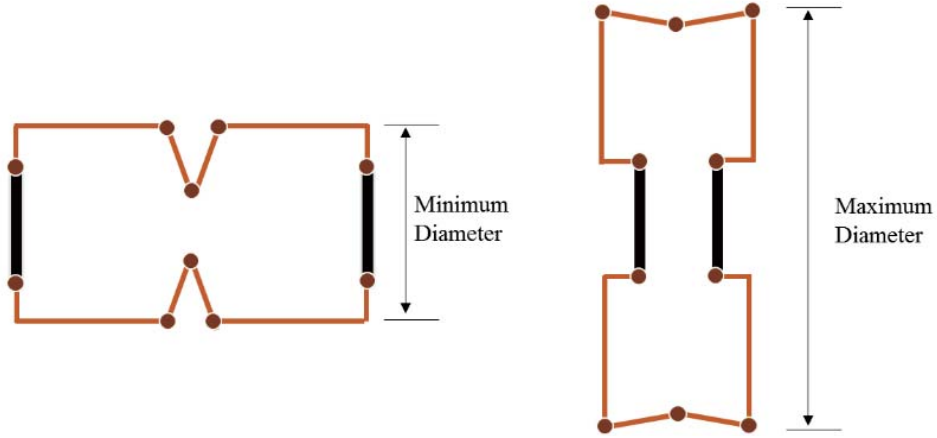


Fig. 2.22. Schematic diagram of the minimum and maximum wheel diameters.

The length of the unit pattern determines the maximum and minimum diameter of the wheel rim. As described in previous section, the wheel rim has three variables— $\rho_{\mathcal{R}}$ ,  $\theta_{\mathcal{R}1}$ , and  $\theta_{\mathcal{R}2}$ —with two constraint equations, (16) and (17). The radius of the wheel - x position of  $A_{R1}$  is

$${}^{\mathcal{R}'}\mathbf{x}_{A_{R1}} = \rho_{\mathcal{R}} + l_u \sin \theta_{\mathcal{R}1} \quad (41)$$

The optimization problem with the constraints was solved by Matlab optimization tool, which reported a maximum value as  $2.56 l_u$  and a minimum value as  $l_u$ . Based on these results, the ideal maximum deformation ratio is 2.56.

To maximize the deformation ratio, other design parameters— $l_h$  and  $l_t$ —should be matched with  $l_u$ . Fig. 2.22 shows a schematic of the wheel in the maximum and minimum states. The minimum radius of the wheel is the summation of  $l_h$  and  $l_t$ , and the maximum radius of the wheel is the summation of  $l_h$  and  $2 l_u$ . Therefore, to achieve the maximum deformation ratio, equation

(45) should be satisfied. In this paper, we set  $l_u$  as 12.5 mm,  $l_h$  as 10 mm, and  $l_t$  as 4 mm.

$$\frac{l_h + 2l_u}{l_h + l_t} = 2.56 \quad (42)$$

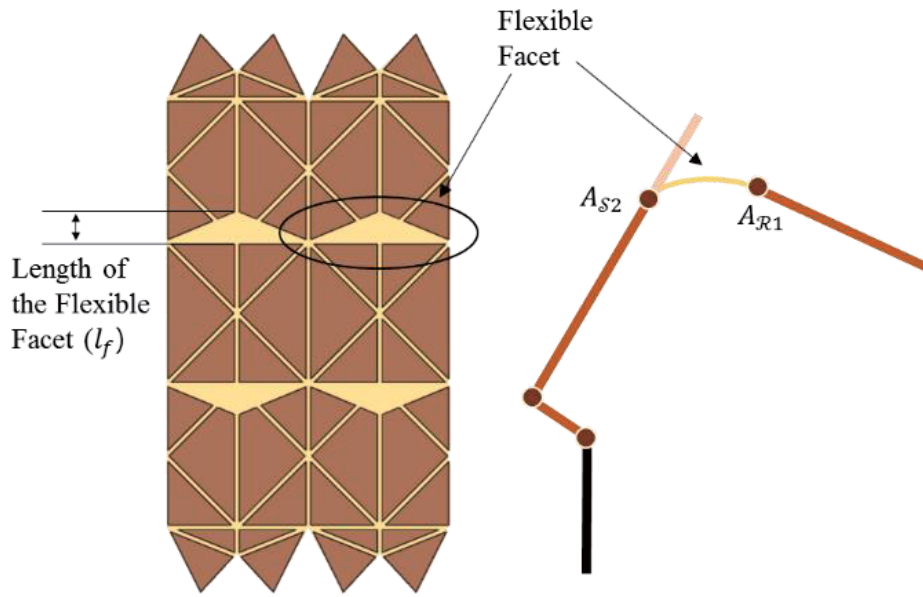


Fig. 2.23. Schematic diagram of the flexible facet.

The size of the flexible facet is another important design parameter. When the size of the flexible facet is too small, the wheel cannot be fully deformed. On the other hand, when it is too large, it weakens the stiffness of the wheel. Fig. shows the schematic diagram of the flexible facet. The position of point  $A_{S2}$  is changed because of the flexible facet. For full mobility, the length of the flexible facet should always be larger than the distance between point  $A_{S2}$  and  $A_{R1}$ . Fig. shows the tendency of the maximum distance to vary as the length of

the flexible facet increases. The coordinate values of the points were computed with Matlab by solving the derived equations in sections 2.2 and 2.3. From the analysis, 4.47 mm of the length of the flexible facet (about 18% of the length of the unit pattern) was chosen as the proper value.

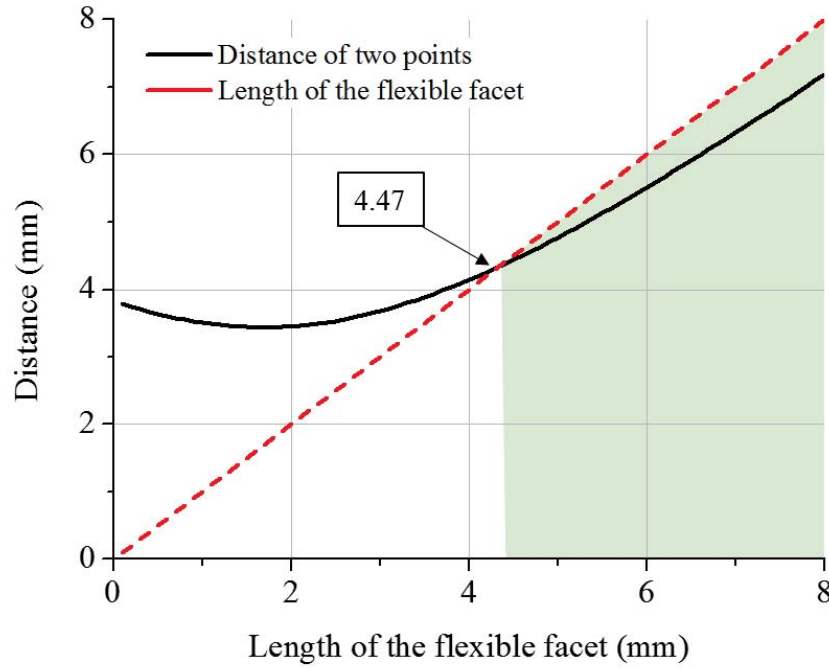


Fig. 2.24. Tendency of maximum distance to vary as length of the flexible facet increases. A value of 4.47 mm of the length of the flexible facet (about 18% of the length of the unit pattern), has been chosen.

## 2.3 Wheel Grouser Design

Using a wheel grouser increases the robot's ability to overcome obstacles by changing the shape of the wheel to function like a rotary leg. The grouser should be assembled robustly to the wheel, and it needs to be folded at the shrunk state and deployed in the enlarged state. To satisfy these conditions, the wheel grousers were attached to facets of the wheel support (Fig. 2.25).



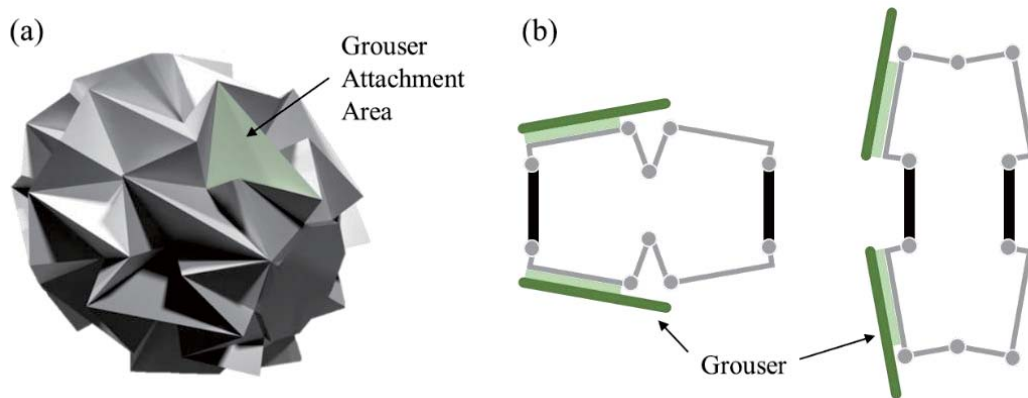


Fig. 2.25. Grouser attachment area (a) and schematic of grouser deployment (b).

Because we used PET material for the facet, a chemical adhesive would not provide reliable adhesive force. Mechanical joining methods such as bolts or riveting are also not appropriate for thin structure like origami. We adhered the grouser with a stapler and adhesive tape. Fig. 2.26 shows the grouser design. The grouser was made with a multi-material 3D printer, which allowed us to design it to have a rubber-like region for stapling and increasing friction. Fabrication details are described in the wheel fabrication chapter.

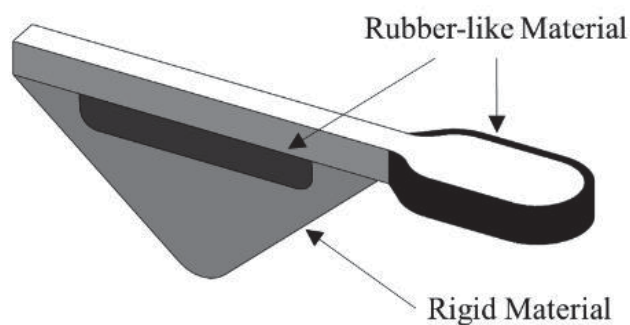


Fig. 2.26. Design of the wheel grouser.

# Chapter 3 Wheel Structure Fabrication

## 3.1. Pattern Embedded Composite

For wheel fabrication, multi-material patterning was adopted rather than single-material patterning to achieve a dramatic stiffness variation between facet and fold line. The material for the facets should be laser-machinable for the patterning, and the material for the folding part should be highly flexible and resistant to fatigue. The delamination problem is one of critical issues in lamination process, and complex patterning on the structure cause more serious problem. To prevent delamination problem, we tried special method that the facet material was enclosed by the fold line material [44, 45]. Adhesive layer between the facet and the fold line material fastened the each layer. Fig. 3.1 shows the total structure.

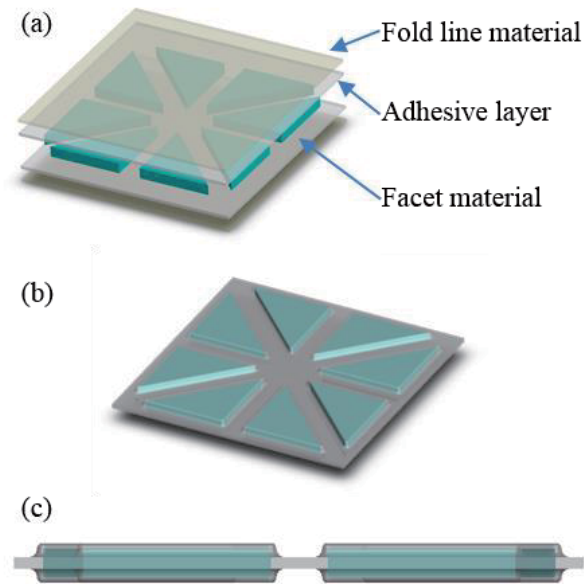


Fig 3.1. Concept design of pattern enclosed composite. The facet materials are machined and enclosed by the fold line material. (a) Structure components, (b) Laminated shape, (c) Side view of result.

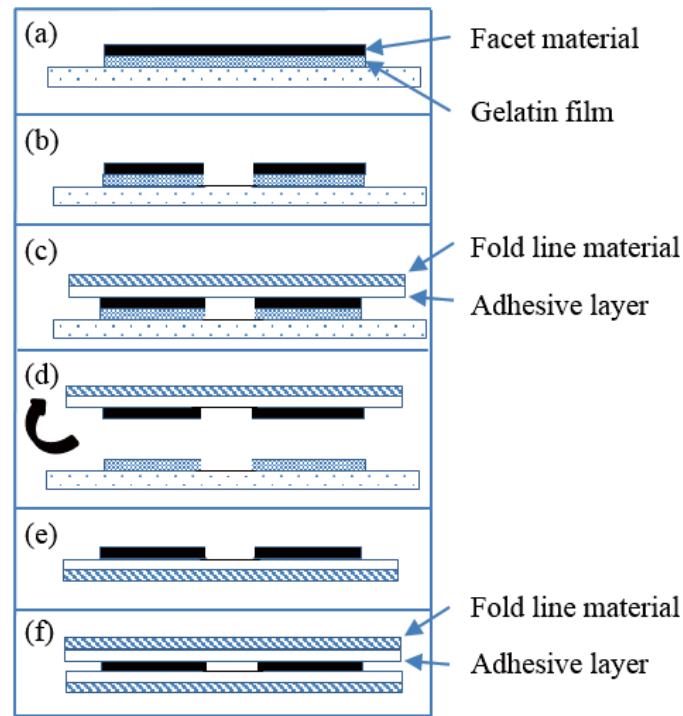


Fig. 3.2 Fabrication procedure of pattern embedded composite.

Fig 3.2 illustrates the fabrication procedure. First, the facet material was placed on the gelatin film plate (a). Gelatin film was used for maintaining alignment. Next, the facet material was machined by universal laser cutter and unnecessary parts were removed (b). In this prototype, spacing between facets was set as twice of thickness of the facet material. And then, the fold line material with adhesive film was placed on the patterned facet material (c). Detaching of the fold line material made separation of facet material from the gelatin film plate (d). Turning it over and laminating another fold line material made final structure (e, f).

Various material can be used as the facet material if it is thin and has high stiffness at the same time. Fig. 3.3 (a) used acrylic plate as facet, (b) used PET film and (c) used polyimide film. The result product had enough robustness and force transmissibility even in complex shape.

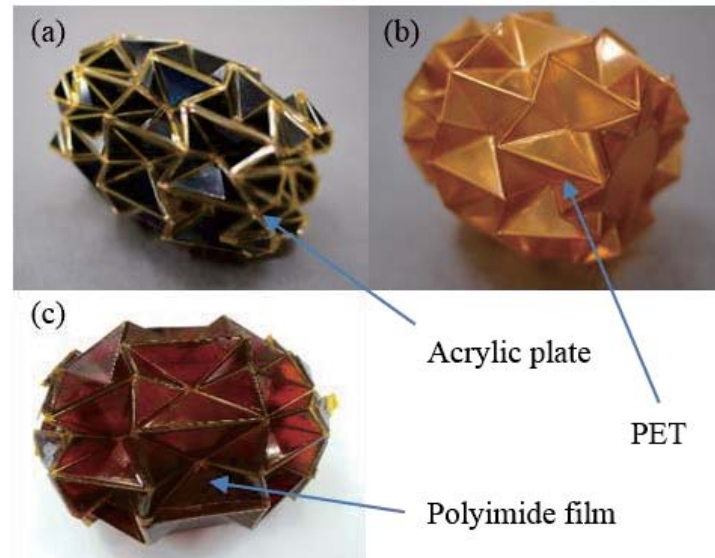


Fig. 3.3. Fabrication result of magic-ball origami pattern using various facet material: (a) Acrylic plate, (b) PET, (c) Polyimide film.

### 3.2. PET Patterning on Mesh Fabric

Enclosing the facet material in the fold line material can solve the delamination problem, but also requires large width of the fold line. Large width of the fold line not only loosen the relative movement of the facet, but also hinder the kinematic analysis of the structure. To solve this issue, the structure was changed that the facet material cover the fold line material, and mesh fabric is used for reinforcing the adhesive force.

A PET film (100  $\mu\text{m}$ , Kolami) with a thermal adhesive on one side was chosen for the facets, and a plain-weave mesh fabric was used for the folding part. The mesh fabric is so pliable that it required very little effort to bend the entire wheel shape but also tough enough to be folded thousands of times. In addition, the thermal adhesive permeates the mesh, which reinforces its adhesive strength.



Fig. 3.4. Wheel fabrication process using mesh fabric.

Fig. illustrates the fabrication process. First, PET film is attached to a weakly adhesive polyamide film (CT-1065, Coretec), which is used to hold the PET film during laser machining (VLS 3.5, Universal Laser System) (a and b). After the unnecessary part of the PET has been removed (c), the mesh fabric is sandwiched between the two processed PET films (d). Because the PET film remains adhered to the polyamide film, it is easy to align the two intricate patterns by hand on a backlight glass (e). In the next step, the sandwiched layers are put into a hydraulic hot press (QM900A, QMESYS) at 5MPa at a temperature of 110°C for 5 minutes and then cooled for 1 hour at room temperature (f). During this process, the resin on the PET film melts and infiltrates the fabric, causing the PET to stick so strongly to the mesh that the facets are hard to peel off the fabric despite many foldings. The polyamide film is then removed from both sides of the quenched substrate (g) and a double-sided adhesive (5316K, Coretec Co.) is pasted to a few parts of the pattern and to the hubs so that they can be fashioned into a wheel shape (h). Before folding up the pattern, grousers are attached using staplers (i). The grousers are 3D printed (Object 260, Stratasys Ltd.) using multi-materials (VeroWhite and TangoBlack, Stratasys Ltd.). The wheel pattern is then folded and assembled with the hub components (j, k). Finally, a rubber band is wrapped around the wheel in the circumferential direction to apply restoring force after folding (l).

Fig. 3.5 shows the final fabricated wheel. The wheel weighs about 9.7 g with the hub components and 4.7 g without the hub components.



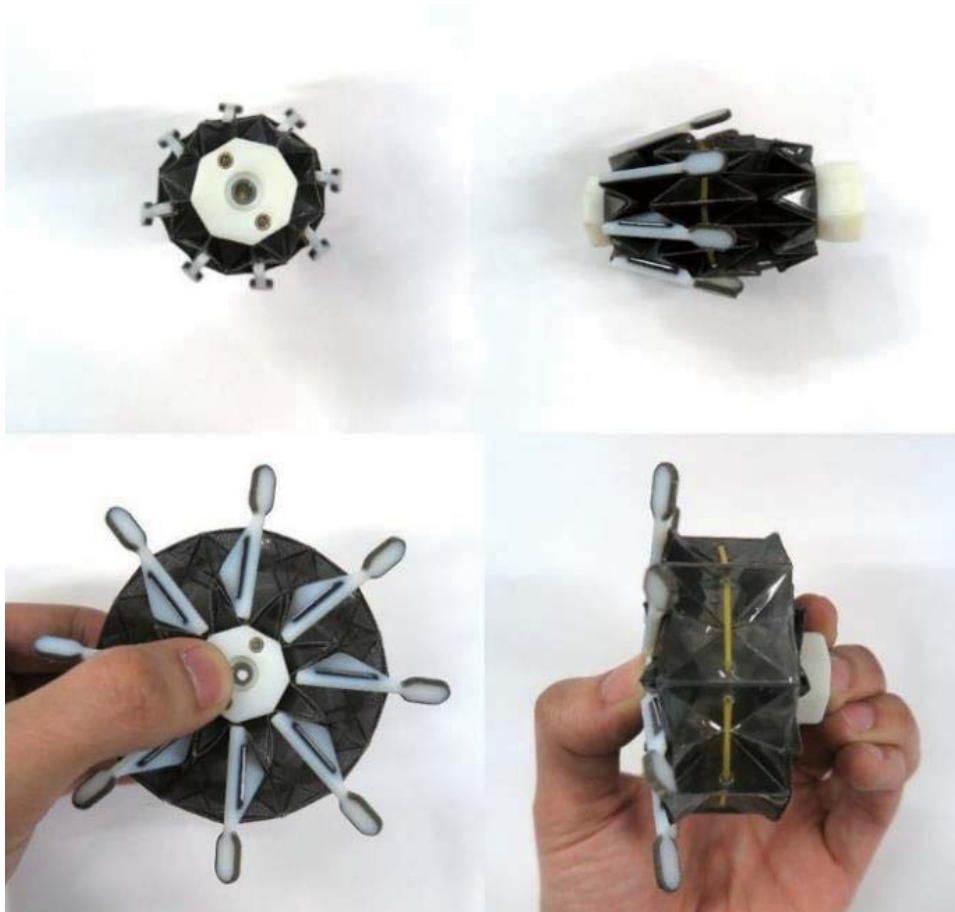


Fig. 3.5. Wheel fabrication results.

### 3.3. Reinforcement of Pattern Embedded Composite

The wheels used adhesive in both lamination of the layers and assembly of the structure. Adhesive makes it easy to fabricate complex patterned structure, but has a problem that it is greatly influenced by environment such as humidity and temperature. In this study, we tried to strengthen pattern embedded composite through mechanical joining method - sewing and bolting. Fig. 3.6 shows the reinforced specimen by sewing. If the fold-line material is the fabric material, it is possible to reinforce the laminating force through sewing on the fold lines.

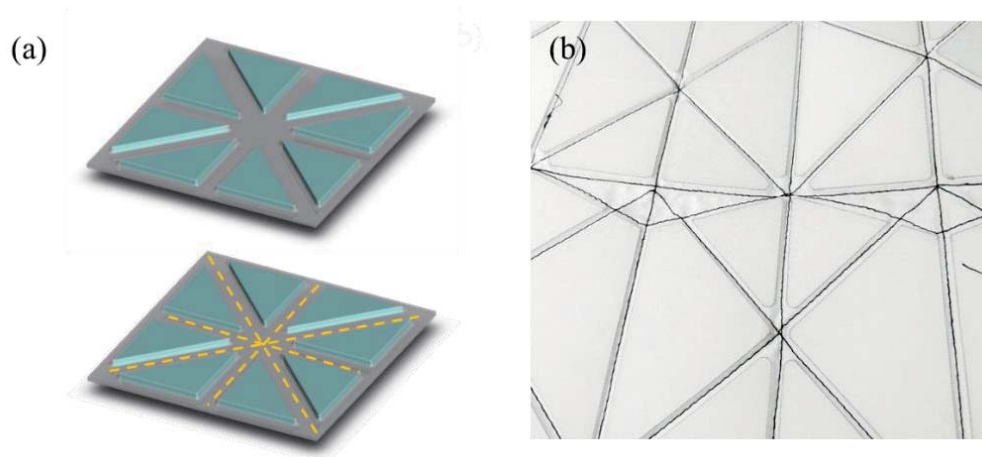


Fig. 3.6. Reinforcement of the laminating force by sewing.

It is also possible to greatly increase the assembling force of the structure by utilizing partial bolting. Fig. 3.7 shows the hub part that needs to be assembled. By utilizing the bolting here, it is possible to solve the problem caused by the adhesive depending on the ambient temperature. The performance changes were discussed in detail in the experimental section.



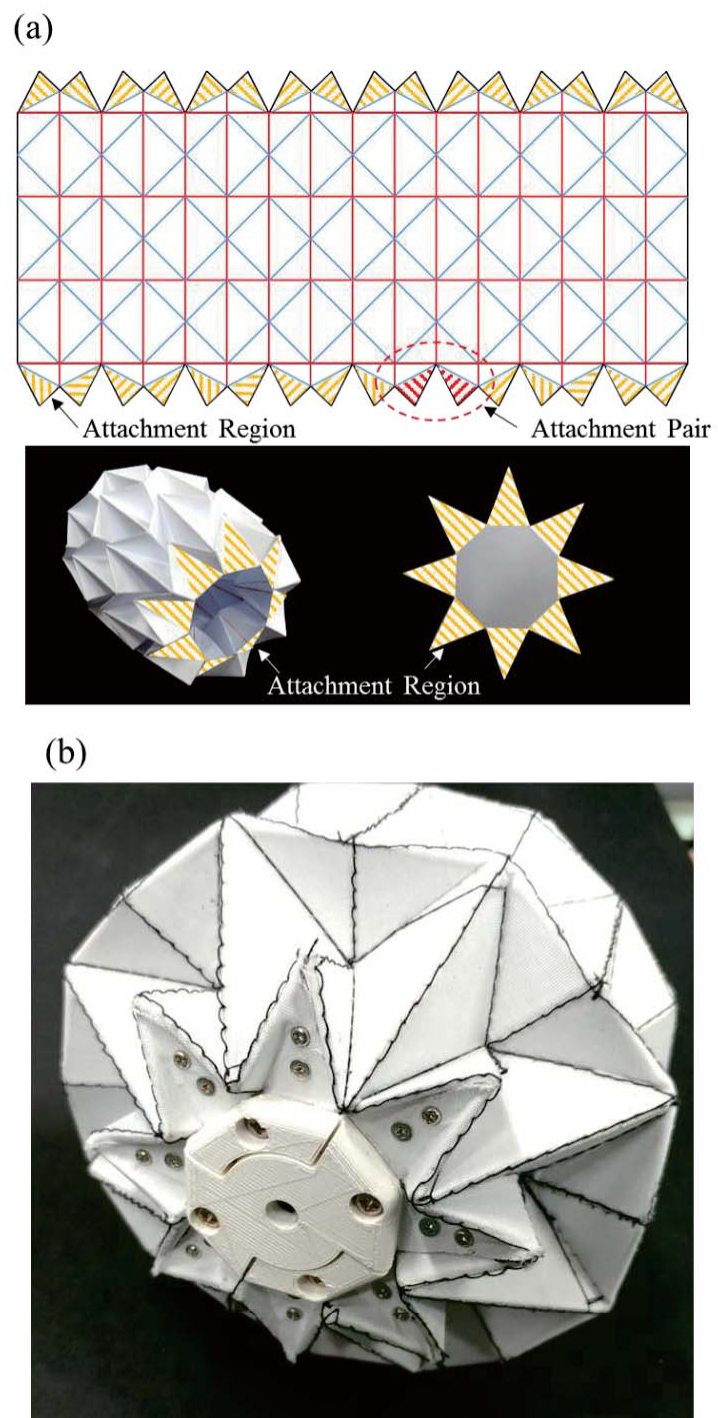


Fig. 3.7. Reinforcement of the assembling force by bolting.

### **3.4. Patterning on Elastomer**

The fabric ensures sufficient durability for repetitive deformation, and it is possible to manufacture wheels with good rigidity using a special purpose fabric such as aramid or carbon based fabric. However, in addition to supporting a load, a wheel must have various functions such as shock absorption and high friction. Therefore, it is necessary to extend the range of materials available as elastomers. In this study, we investigated the possibility by using a urethane series elastomer Vytaflex40 (Smooth-on). The material used for facet is cardboard paper.

Fig. 3.8 shows the fabrication process. Cardboard was fixed on gel pack and patterned by laser machining. Urethane was poured and cured to make patterned specimen. Cured specimen was assembled using bolting to wheel shape.

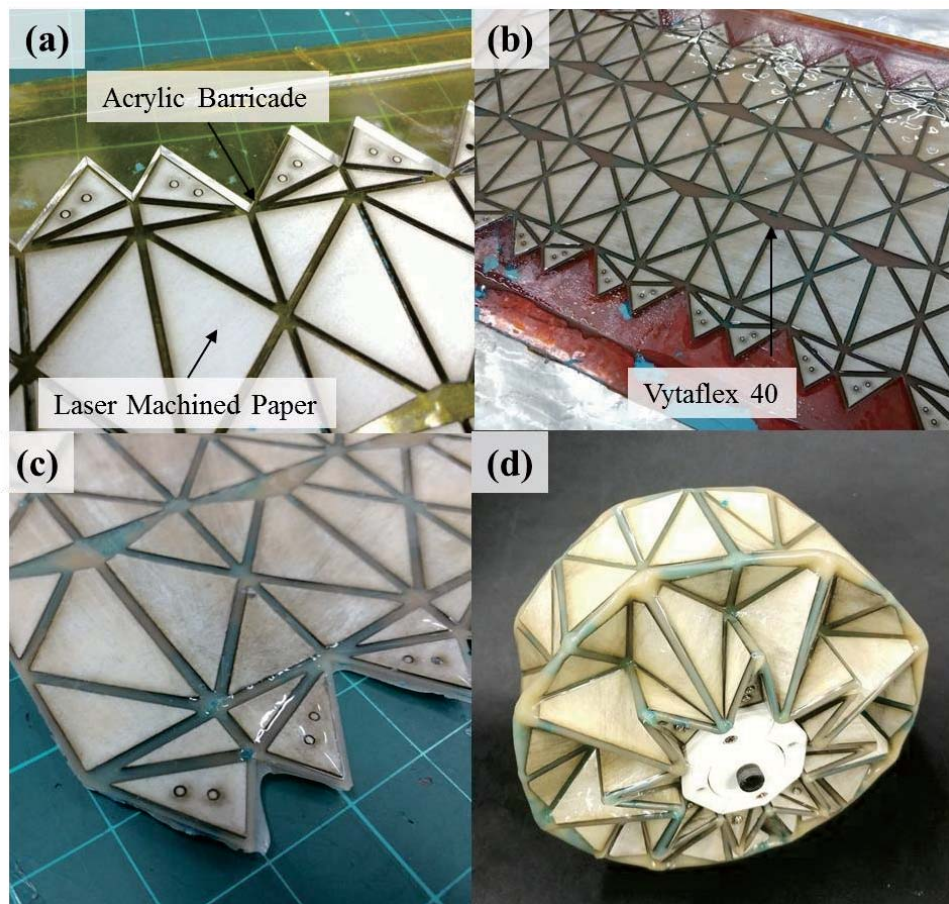


Fig. 3.8. Fabrication of elastomer (urethane) based wheel structure.

# Chapter 4 Robot Platform Design

## 4.1. Wheel Deformation Mechanism

### 4.1.1. Multi-Shaft Mechanism

The diameter of the wheel is varied by changing the length of the wheel in the direction of the axis. Fig. 4.1 shows schematics for two basic ways to do this: moving the inside wheel hub and moving the outside wheel hub. To allow for relative motion of the hub, at least one side of the wheel should be adjustable.

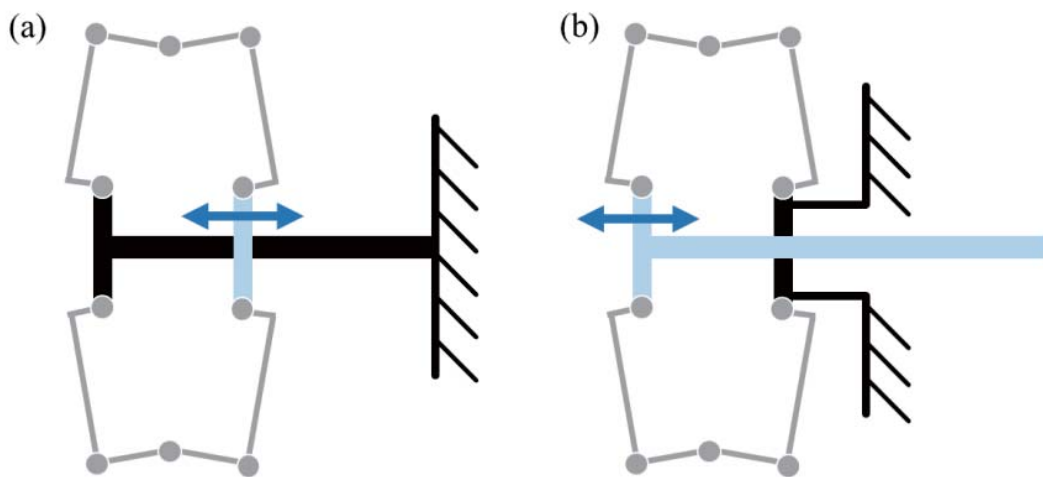


Fig. 4.1. Two different methods for varying wheel diameter.

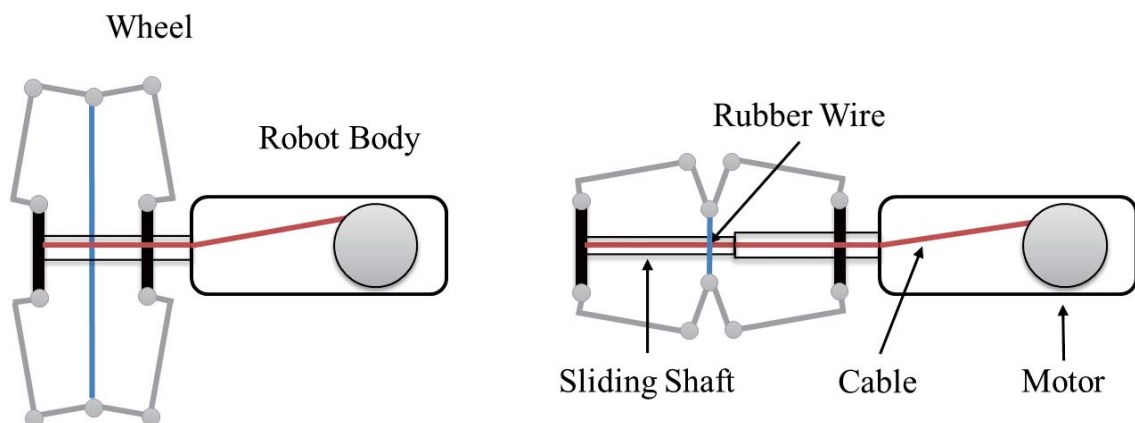


Fig. 4.2. Wheel transformation mechanism using sliding shaft.

We chose to use the second method with sliding shaft to reduce the applied bending moment on the shaft (Fig. 4.2). Sliding shaft enables wheel deformation, but the rotation of the wheel cause the cable twisting problem. To prevent the cable twisting, the multi-shaft structure is introduced.

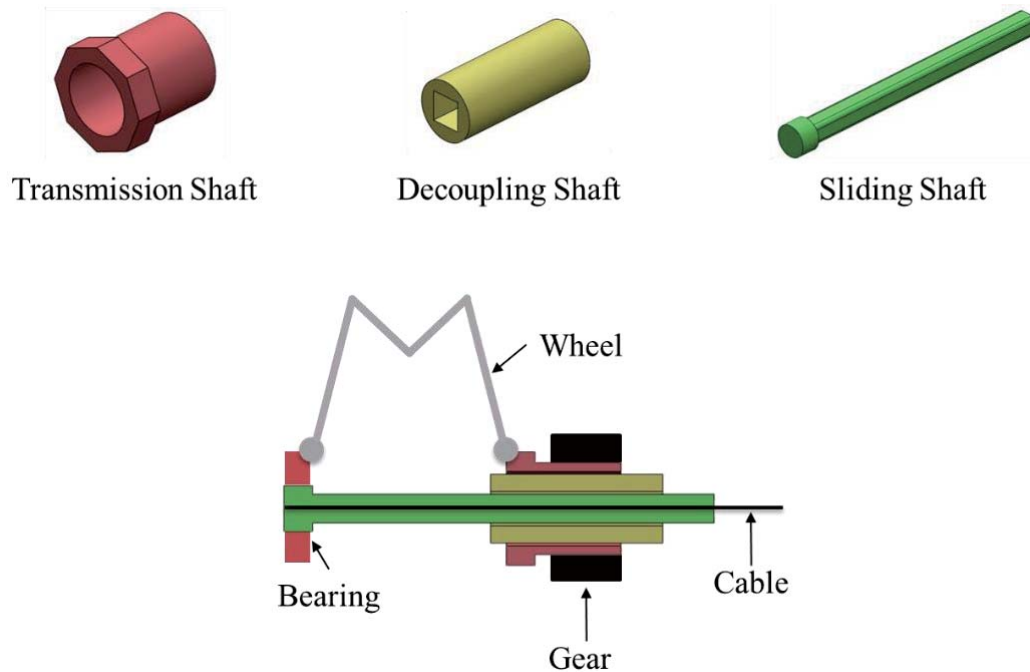


Fig. 4.3. Multi shaft structure for cable twisting problem. The middle shaft decouple the sliding shaft and the torque transmission shaft.

The multi-shaft structure can decouple the sliding movement with the rotational movement (Fig. 4.3). Outer shaft – transmission shaft transmit the torque from the motor to the wheel and is fixed to one side of the wheel. Middle shaft – decoupling shaft prevent the rotation of sliding shaft and is fixed to the robot body. Inner shaft – sliding shaft is connected with the wire and fixed to the outer side of the wheel with bearing thereby it can transmit the deformation force without rotation.

#### **4.1.2. Flexible-Shaft Mechanism**

The proposed structure can prevent cable twisting problem, but this method requires a large internal space to allow the shaft to slide with the stroke. According to the wheel dimension selection in the wheel design chapter, each shaft requires at least 40 mm of internal space in a robot body.

To reduce the required internal space, we replaced the rigid shaft with a flexible one. The flexible shaft is connected to the outside hub via a bearing, so the shaft can pull the outside hub when the shaft pulley winds it up (Fig. 4.4). To ensure low resistance force during winding, a material with low bending stiffness is preferred. However, a low-stiffness material is susceptible to twisting because the wheel should be rotating.

To solve the problem, we used an anisotropic structure that has low bending stiffness and high torsional stiffness: a coil spring with a wire in its center (Fig. 4.4 [a]). Coil springs have low bending stiffness and relatively high torsional stiffness, so the shaft can be wound up on the pulley without twisting. The wire prevents extension of the coil spring. The elastic band encircles the wheel to recover the original shape when the shaft tension is released.

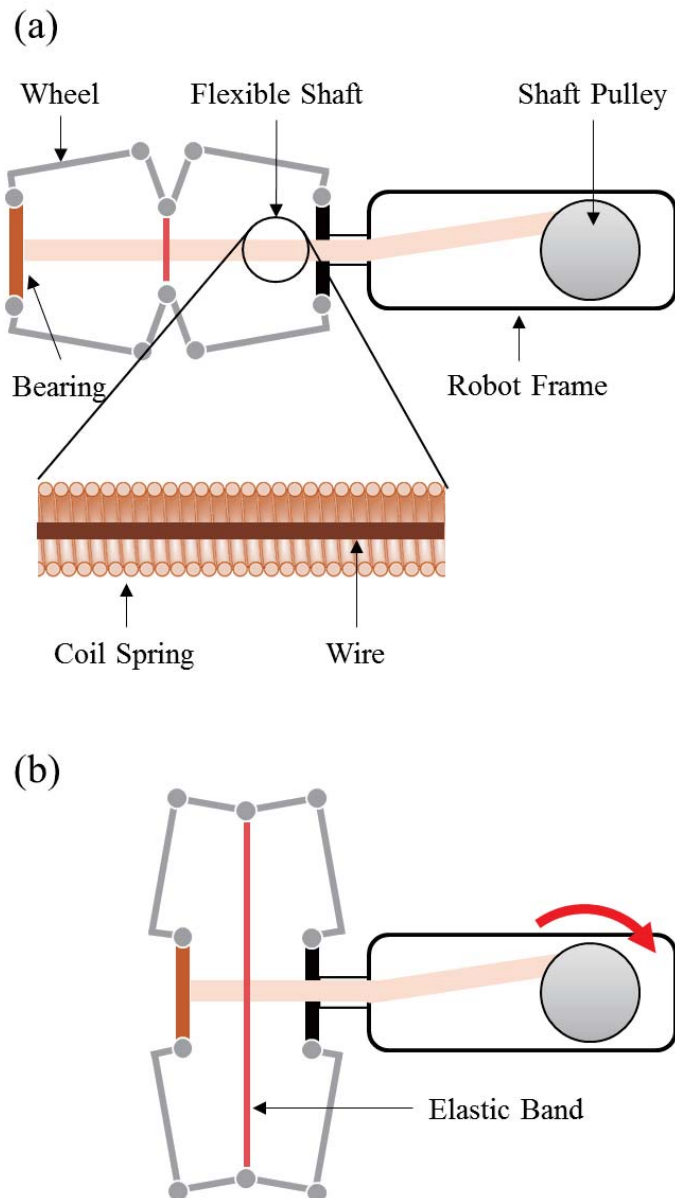


Fig. 4.4. Schematic of the wheel deformation mechanism using a flexible shaft. The coil spring allows the shaft to be wound up on the pulley and prevents twisting. The internal wire prevents extension of the coil spring.



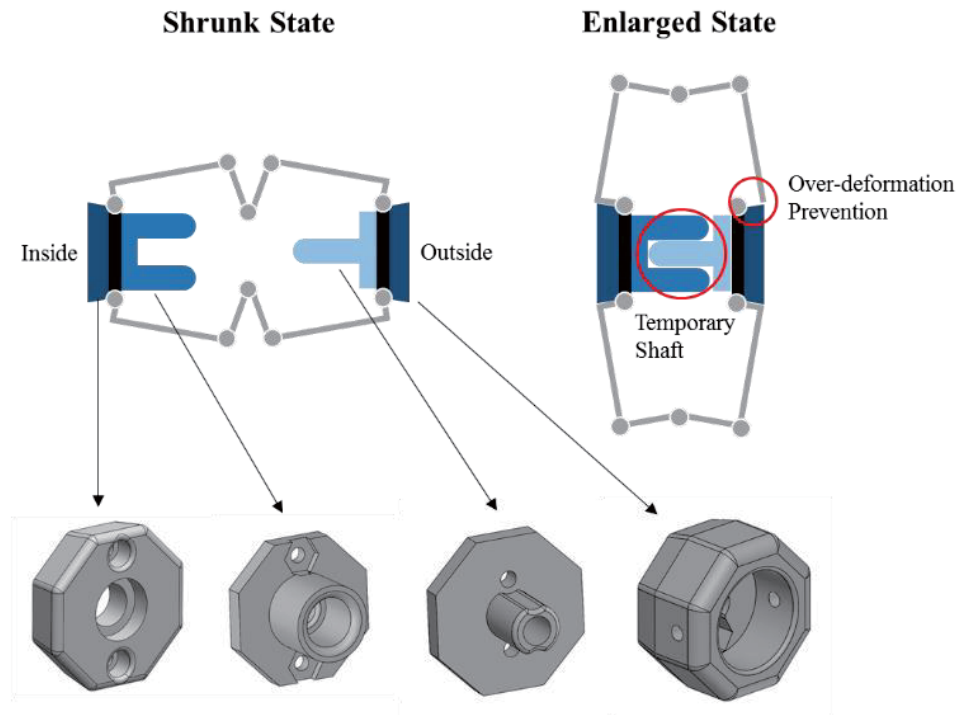


Fig. 4.5. Wheel hub design for the axis misalignment problem.

Another issue with using a flexible shaft is the potential for wheel axis misalignment. This happens when the flexible shaft structure cannot hold the position of the outside hub. In the shrunk state, bending the wheel axis causes only a small variation in the contact height of the wheel with the ground, but in the enlarged state, the problem became significant. To prevent this problem, a specially designed hub structure was built (Fig. 4.5). The outside hubs prevent over-deformation of the wheel. The inside hubs are assembled at the enlarged state, and in this configuration they function as a shaft. These components create a stable wheel configuration.

For the path of the flexible shaft, the driving motors transmit rotation torque to the wheel via gears. Fig. 4.6 shows the detailed design and overall view of the robot. The robot has two deformable wheels on both sides and a carriage



tail for the electronics and batteries. The tail structure is also necessary for obstacle climbing. For driving the wheel, 1.5 W DC motors (1224E 256:1, Faulhaber) were used, and for wheel deformation, the identical motor with an encoder was used. Fig. 4.7 shows the assembly view and components for the deformation mechanism. The body structure was separated into two parts for assembly.

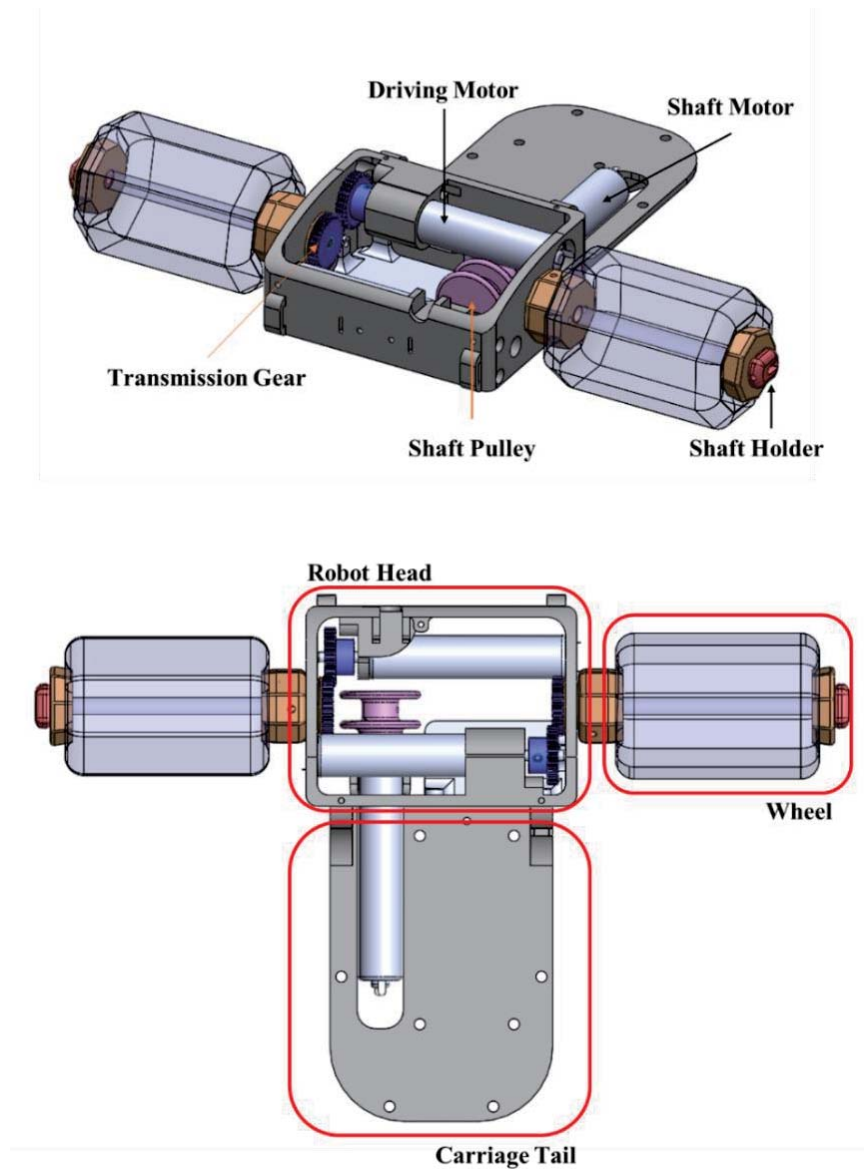


Fig. 4.6. Overall view of the wheel deformation and torque transmission mechanisms.

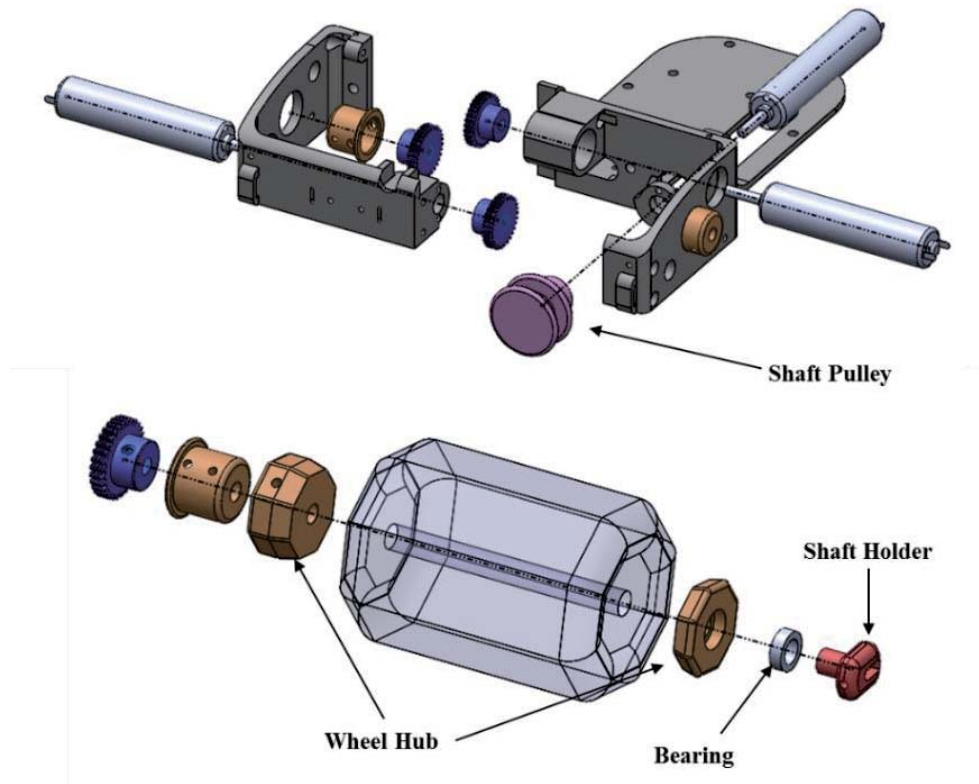


Fig. 4.7. Assembly view and components of the wheel deformation mechanism.

## 4.2. Electronics and Interface

Fig. presents the control schematic for the robot. The control interface was built with a commercial WIFI camera module and an Arduino Nano controller. The WIFI camera module (P5206-2, HanJin Data) can be connected with a smartphone application (offered by HanJin Data) via WIFI, so the user can see real-time video and also send a command. The WIFI camera module provides user commands via UART communication using a preset data protocol. An Arduino Nano was used for the main control unit. Arduino Nano interprets user commands from the WIFI camera module and combines them with an encoder signal to control the motors.

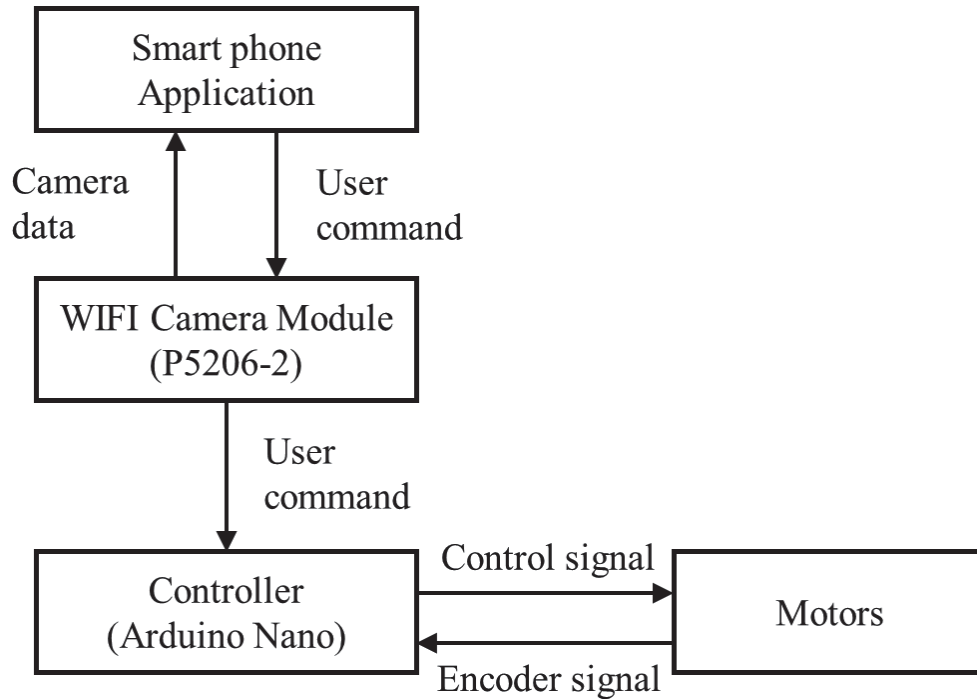


Fig. 4.8. Control interface block diagram.

### 4.3. Robot Fabrication

All structural components of the robot were fabricated with a 3D printer (Objet 260, Stratasys Ltd.) (Fig. 4.9). The communication module, cooling fan, and battery for the controller were placed on the head side, and the main controller and battery for the motors were placed on the carriage tail. A PET cover was placed on the robot body to protect body components. Fig. 4.10 shows the final robot, which weighs 278 g with batteries.

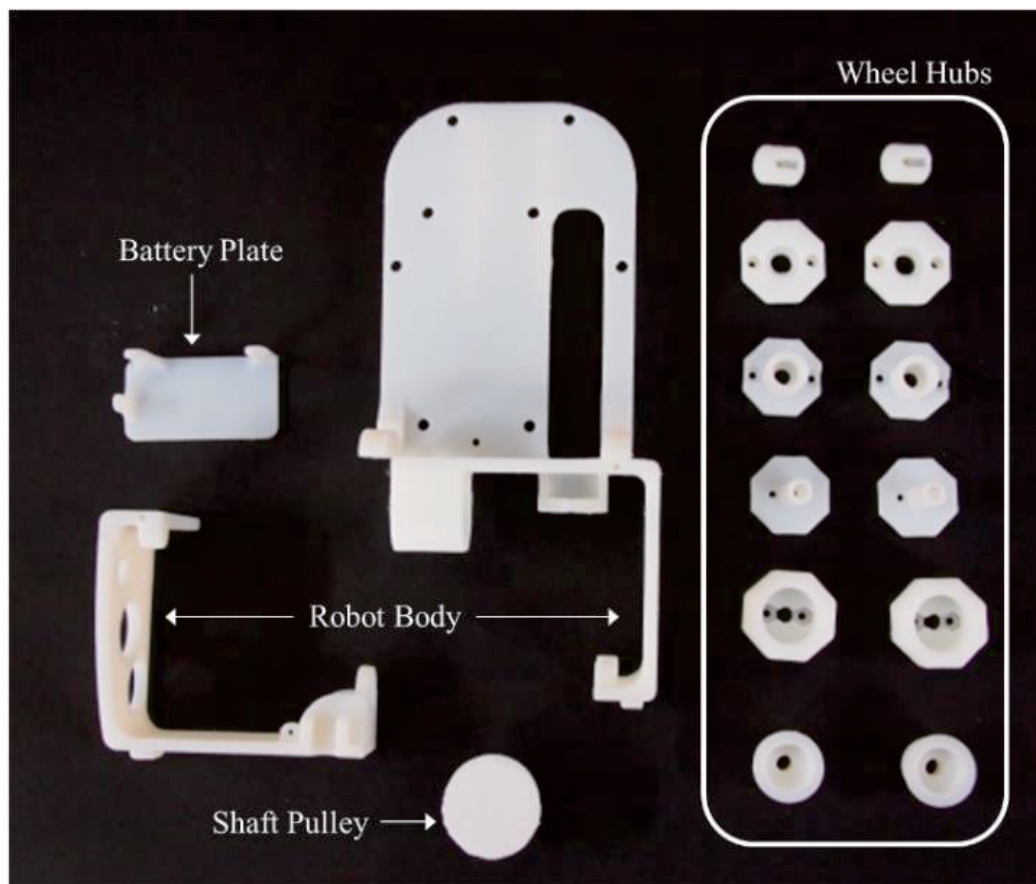


Fig. 4.9. 3D printed robot components.

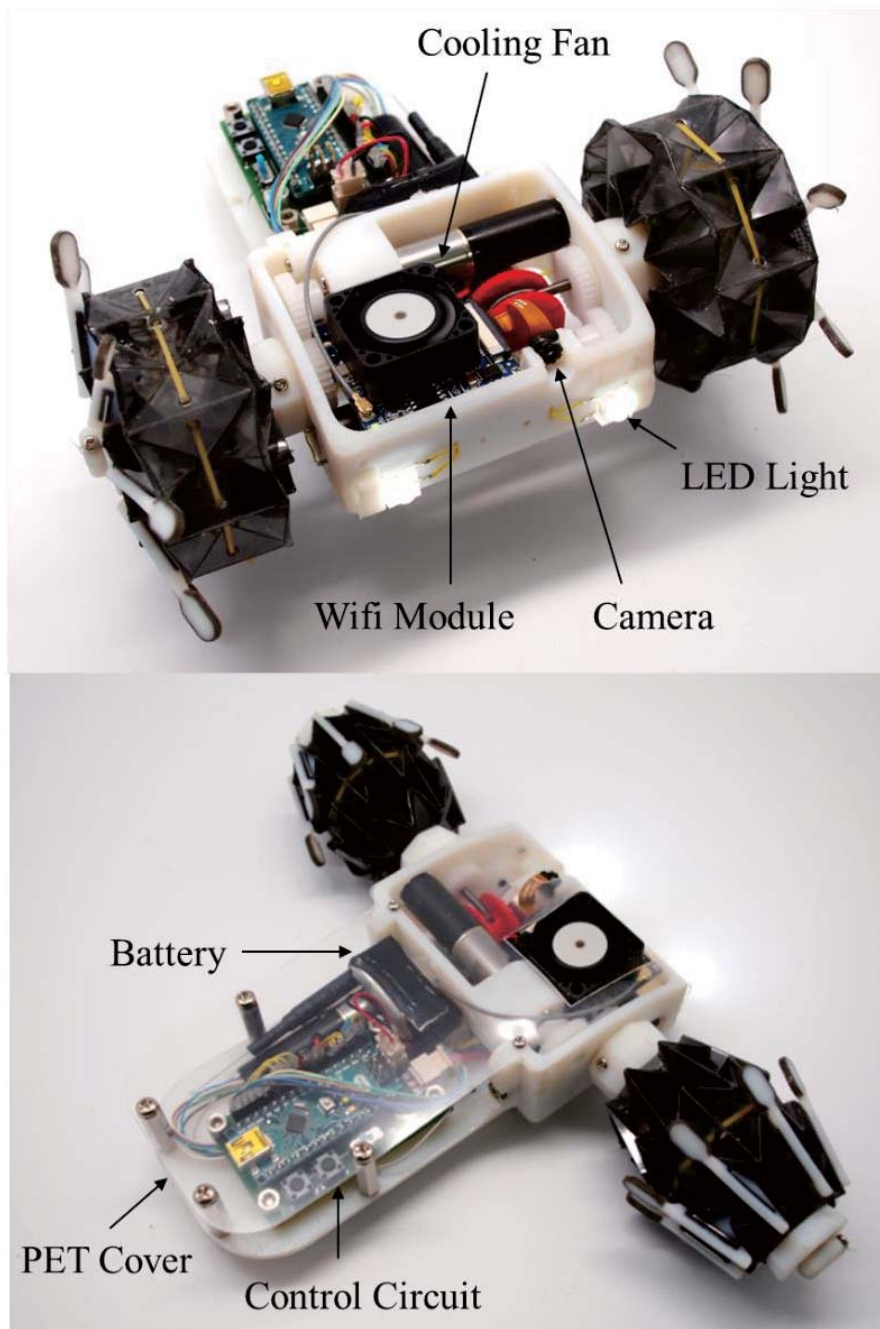


Fig. 4.10. Final assembled robot.

# Chapter 5 Experiment and Result

## 5.1. Wheel Characteristics

Although the mechanism can move with zero kinematic mobility because of the compliance of the materials, the effect of the flexible facet on wheel performance is considerable. In this section, we define two performance factors and investigate the effect of the flexible facet.

The first performance factor is related to the energy required for deformation. A soft robot is composed of a soft and elastic material, so the transmission of a soft robot also contains softness: Movement of the mechanism is induced by material deformation and increases the internal energy. Because of this, output movement per input energy can be an important performance factor for the robot. To investigate this, we introduced a performance factor called “deformation cost” that represents the required energy per unit output movement. In this case, the output movement is variation of the diameter of the wheel, and the input energy is the pushing force of the wheel hub. The deformation cost factor usually shows a non-linear response, so we used the average value. We calculated the overall input energy by integrating the pushing force by the displacement from the initial state to the maximally enlarged state and dividing it by the total diameter variation.

The second performance factor is related to sustainability of the structure. The materials used to make soft robots usually have a large elastic region and low stiffness, which causes considerable deformation in response to an applied force. Therefore, both structural stiffness and maximum payload in a target direction are important performance factors, especially when an application

needs to endure high force, such as a wheel. We applied force in a radial direction and measured initial structure stiffness (in 5% linearity) and maximum payload.

For the experiments, four types of specimens were prepared. Different types of specimens had different ratios of the flexible facet  $\gamma_f$  (0, 6, 18, 30%), and the other wheel dimensions were the same as those specified in section 2.4. Each specimen represents the wheel without flexible facet (0%), with small flexible facet (6%), with theoretically appropriate flexible facet (18%) and with excessive flexible facet (30%). In section 2.4, 18% of the ratio of the flexible facet is theoretically expected for achieving mobility of the wheel structure.

Fig. 5.1 shows the experimental setup to measure the force for the wheel diameter variation. The wheel was pushed in the direction of the axis by a tensile tester (RB302, Unitech) at a constant speed of 20 mm/min, and the pusher connected to the load cell measured the axial force at a collection speed of 3 Hz.

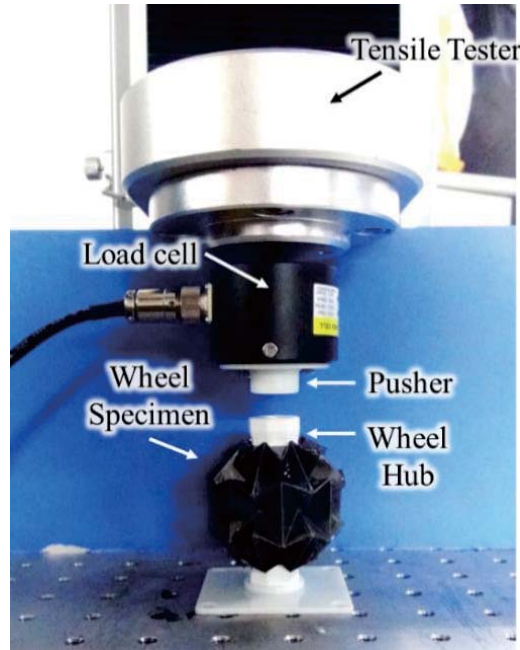


Fig. 5.1. Experimental setup for the wheel diameter variation.



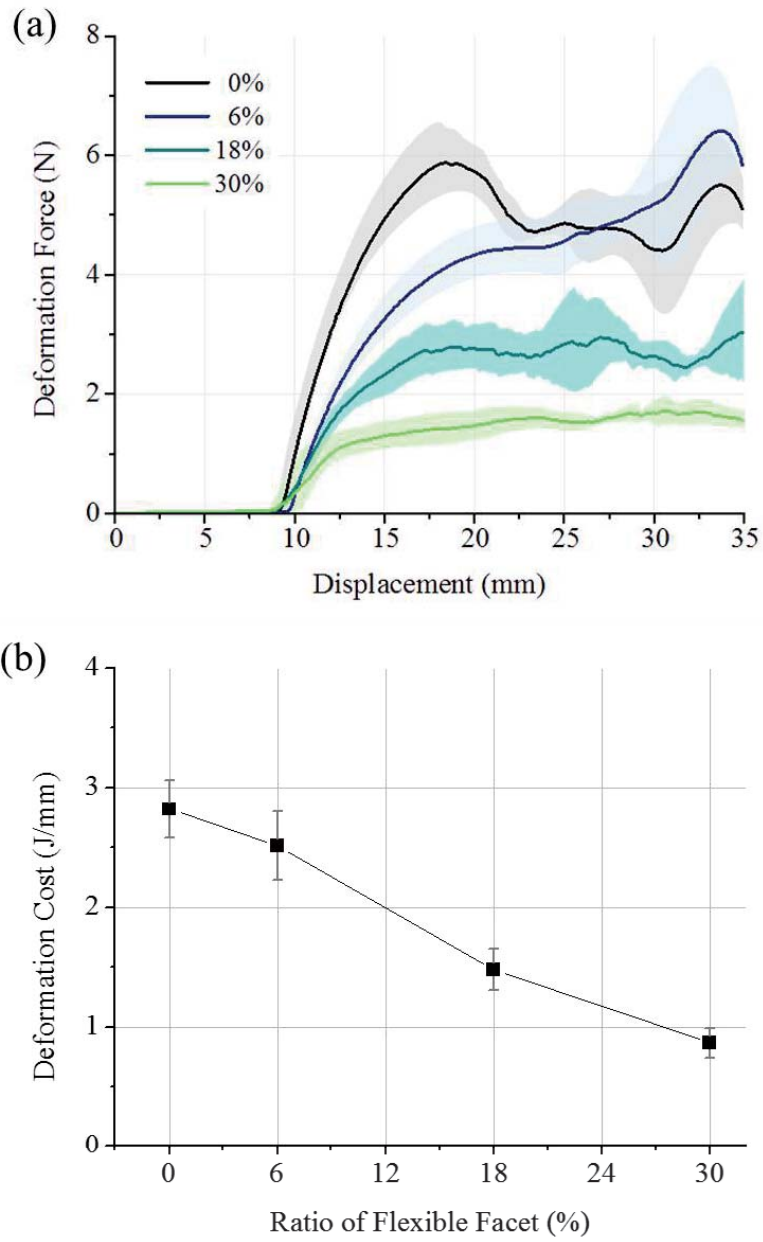


Fig. 5.2. Experimental results of the wheel diameter variation. The graph (a) is a force-displacement profile for wheel deformation, and the graph (b) shows deformation cost. The area in graph (a) presents a  $\pm 1$  standard deviation. The existence of flexible facets dramatically reduces the deformation cost and standard deviation.



Fig. shows a force-displacement profile for wheel deformation (a) and deformation cost (b). Four copies of each type of specimen are prepared, and all experiments are repeated twice. Both graphs present a  $\pm 1$  standard deviation. Theoretically, the deformation cost should be saturated at 18%, but the stiffness of the flexible facet causes a consistent decrease in the deformation cost. The expectation comes from the assumption that the facets have infinite stiffness and the flexible part have zero stiffness, so the results cannot be perfectly matched with the theoretical expectation. Still, it is possible to extract some characteristics of the flexible facet from the results.

First, the flexible facet dramatically reduces the deformation cost, which can be interpreted to mean that the flexible facet reduces distortion of the material. Second, the flexible facet also reduces variation of the deformation cost. High variations in the results derive from the constrained movement of the mechanism. Therefore, low standard deviation can be interpreted as indicating that the mechanism has mobility.

Fig. 5.3 shows the experimental setup for measuring the maximum wheel payload. Each wheel specimen was placed with the shaft in a fixed configuration that maintained the distance between the two hubs at 45 mm, and both ends of the shaft were fixed to the linear guide. The wheel was pushed at a constant speed of 20 mm/min in the radial direction (y-direction in this setup) by the tensile tester (RB302, Unitech) through the shaft connected to the linear guide, which minimized friction force during pushing. The load cell collected the force data during pushing with 3 Hz, and we measured the maximum payload that the specimens could sustain before breaking.

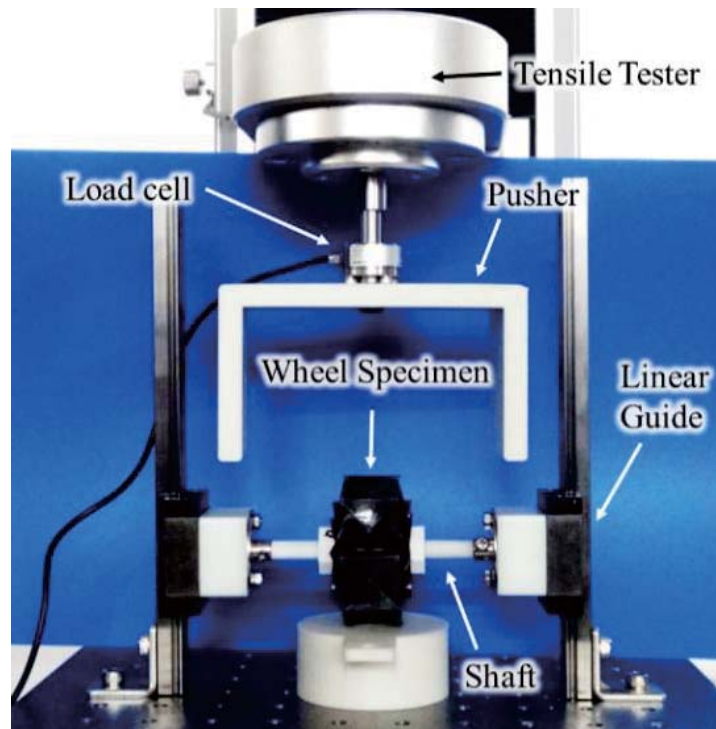


Fig. 5.3 Experimental setup for wheel payload.

Fig. 5.4 shows the results of the payload test. Four copies of each type of specimen are prepared, and all experiments are not repeated because of structural failure. Both graphs present  $\pm 1$  standard deviation. The maximum payload was measured at the point when the wheel supports collapsed. When the specimen had no flexible facets, the wheel had high instability and easily collapsed to one side. These specimens showed low maximum payload and initial stiffness with high standard deviation compared to other specimens even though they had the highest deformation cost. As the length of the flexible facet increased, the wheel became stable and the maximum payload and initial stiffness also became high, but large flexible facets cannot hold the structure firmly and make the wheel easy to collapse. In the robot, 18% of the flexible facets are used, which shows about 41 N of the maximum payload, which is more than 400 times the weight of the wheel structure.

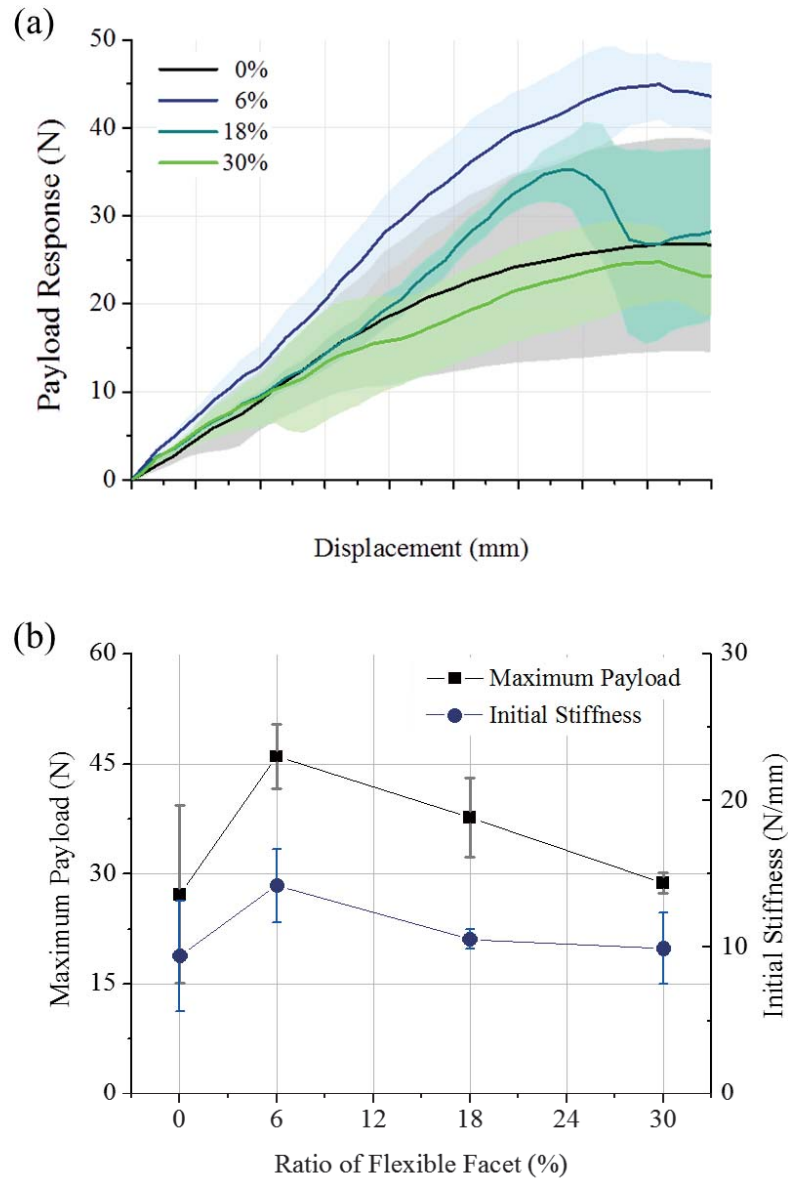


Fig. 5.4. Experimental results of the wheel payload test. The graph (a) shows the force-displacement profile for the wheel payload response, and the graph (b) shows the maximum payload with initial stiffness (in 5% linearity). As the length of the flexible facet increases, the wheel become stable and maximum payload and initial stiffness also become high, but beyond a certain length a large flexible facet cannot hold the structure, and it collapses easily.

As discussed in the wheel fabrication section, the adhesive is significantly affected by the ambient environment. To solve this problem, we propose a method to increase laminating force and assembling force by sewing and bolting. In this section, the effectiveness of this method is demonstrated by measuring how the payload of the wheel changes at various temperatures.

Fig. 5.5 shows the experimental setup. In order to compare the performance of the reinforced specimen, the wheel specimen made of pattern embedded composite method was used in this experiment unlike the previous experiment. The heat was applied by the heat chamber and the low temperature was achieved by cooling through dry ice.

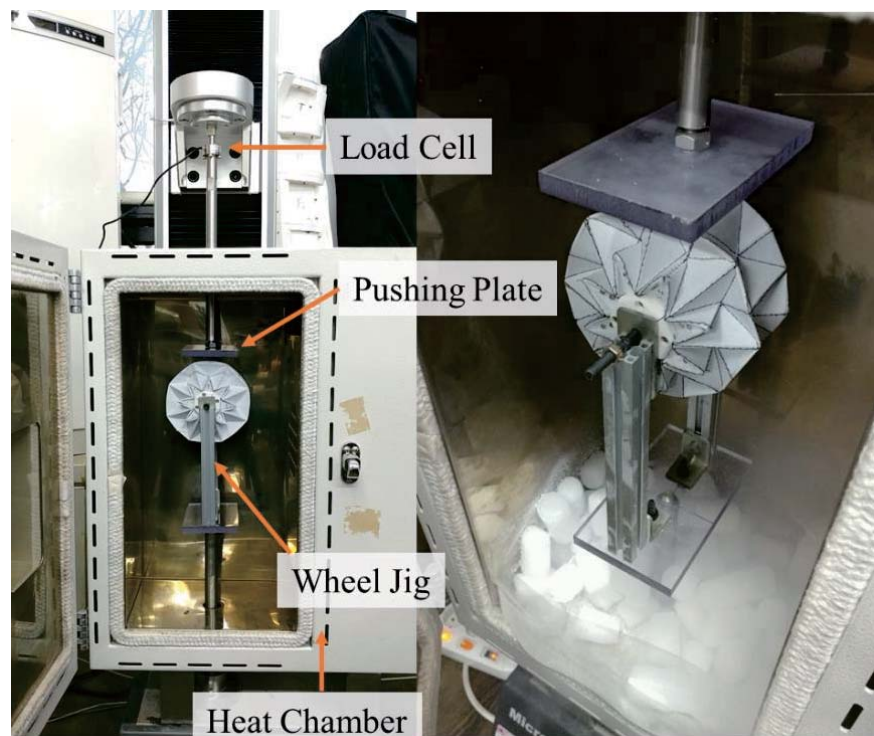


Fig. 5.5. Experimental setup for payload test at various temperature.

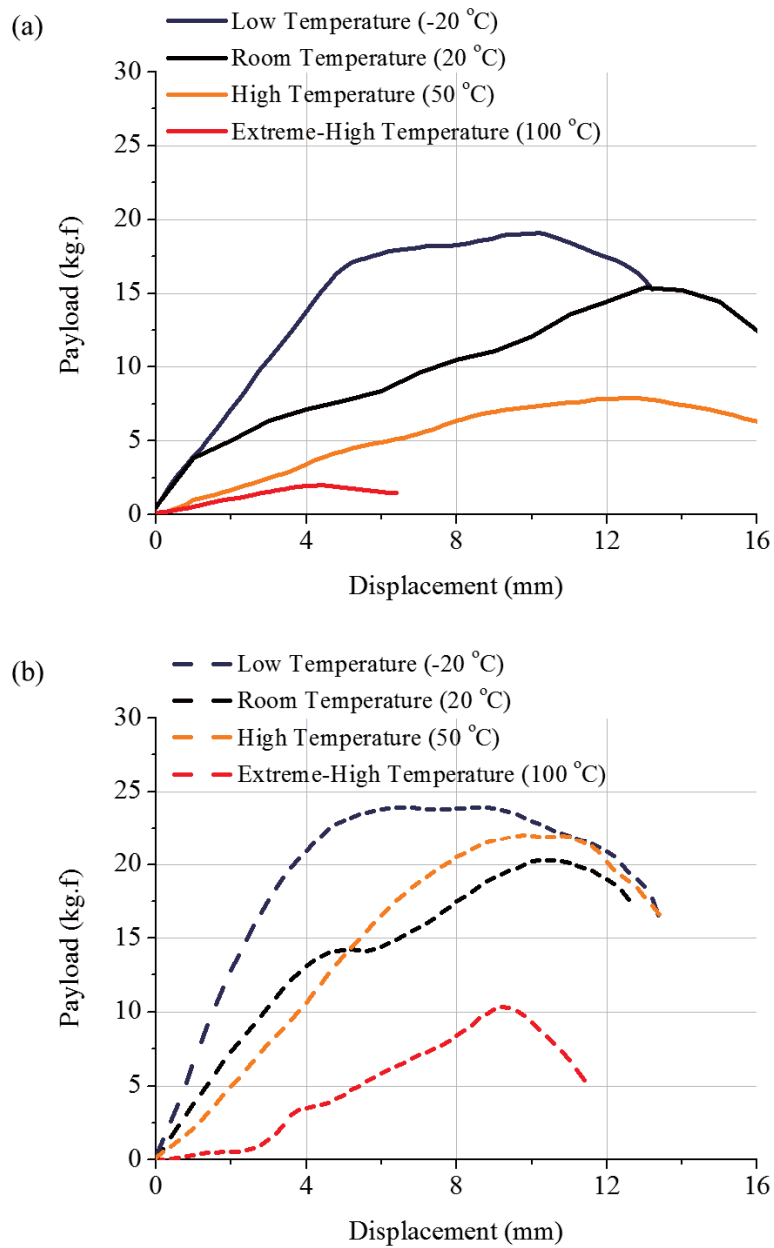


Fig. 5.6. Experimental results of the wheel payload test at various temperature. (a) presents the result of the original specimen and (b) presents the result of the reinforced specimen.

Fig. 5.6 shows the experimental results. (a) is the result for the original specimen, and (b) is the result for the reinforced specimen. Original specimens showed a large performance drop in 50 °C and 100 °C. For the reinforced specimens, the performance was maintained at 50 °C and showed a decline at 100 °C. In the case of low temperature, both specimens showed high performance, which seems to be caused by the freezing of facet material.

Fig. 5.7 presents a comparison of the performance of two specimens at various temperature. The reinforced specimens showed superior performance over all temperature ranges and showed that they could be used without degradation at temperatures ranging from -20 °C to 50 °C.

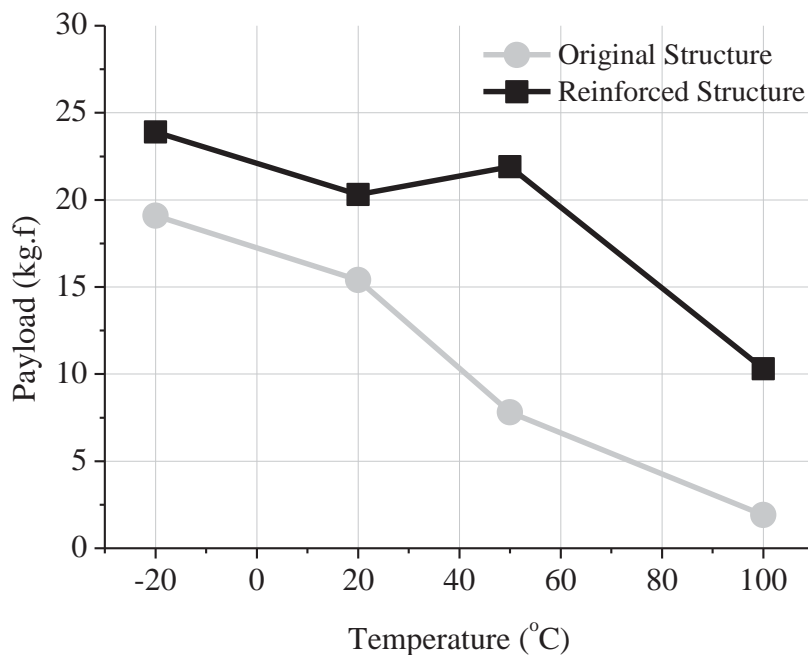


Fig. 5.7. Payload comparison at various temperature.

## 5.2. Robot Performance

Fig. 5.8 shows wheel diameter variations for the robot. When the wheel is maximally enlarged, the diameter is 68 mm without the grouser and 90 mm with the grouser. When the wheel is maximally shrunk, the diameter is 30 mm without the grouser and 45 mm with the grouser. By alternating the wheel diameter between these two states, the robot can climb a 50 mm step and pass over a 50 mm gap. Fig. 5.9 shows frames from a videotape of the robot navigating these obstacles.

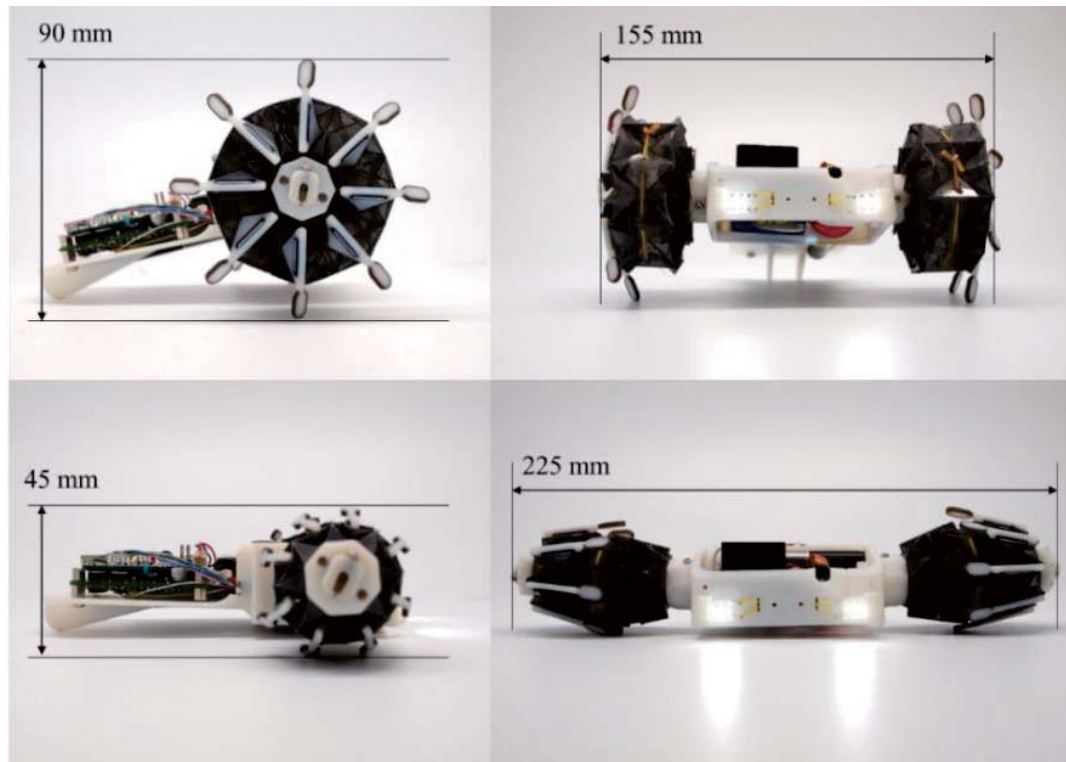


Fig. 5.8. Wheel diameter variations of the robot.



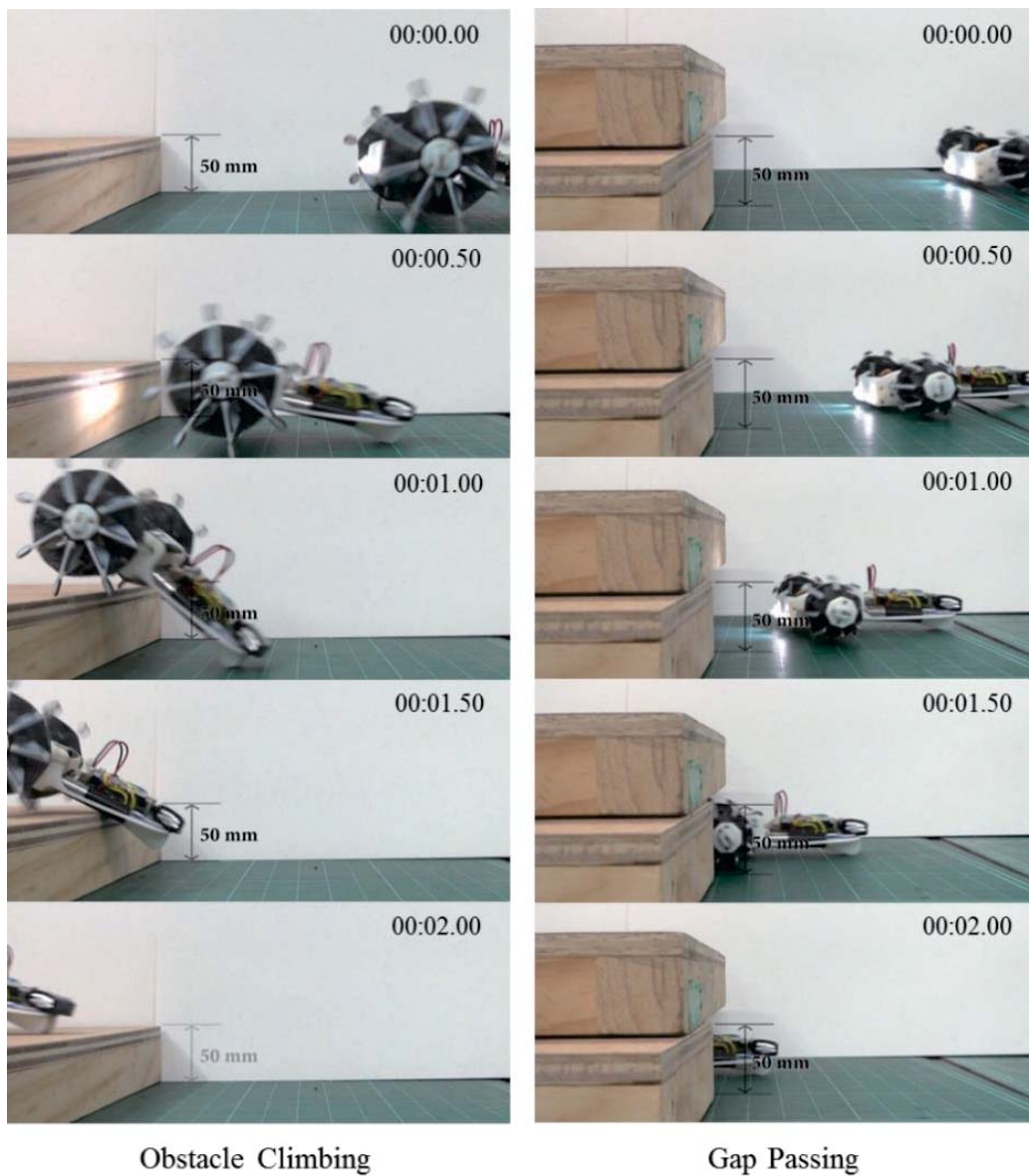


Fig. 5.9. Video snapshots of the maneuverability performance test.



## Chapter 6 Conclusion

Through the thesis, a soft robotic application for a deformable wheel was proposed. The wheel is an example of a mechanical component that needs to be able to endure high external force. To accomplish this with a soft robotic design approach, we applied origami patterning and tuned the overall behavior of the wheel by segment stiffening. As a result, we developed a lightweight wheel (about 9.7 g) that can deform in size by more than twice its original diameter and deliver a relatively high payload of more than 400 times its weight.

Although the research is at the initial state in regards to practical use, we believe that the proposed concept has high potential to be a new type of airless tire based on origami inspired deformable structure. We expect that this new type of tire can be applied to various wheeled applications that require high mobility from a home service robot to a personal mobility. There can be three barriers in expanding the application fields of this concept - deformation ratio, size limitation, and maximum payload.

The first topic is about the deformation ratio. The proposed design used the identical repeated unit pattern and the repetition number is fixed by  $3 \times 8$ . Under these conditions, it was possible to find the optimal design parameter for the deformation ratio based on the kinematic analysis. Increasing the repetition number of the pattern will increase the maximum diameter of the wheel without change of the minimum diameter, but it could make the structure more pliable by providing additional freedom. Changing the shape of the unit pattern is also an interesting issue for improving the performance of the wheel. The square unit pattern can be replaced by rectangle or parallelogram. The variation of the

unit pattern shape will allow the hub, support, and rim part to have their own functional design.

The second topic is about the size limitation. Origami structure is basically scalable because of a frictionless joint which is one of important advantages of origami based mechanism. The proposed wheel, however, has multiple stacking folding part and is also composed of multi-material. The size limitation comes from material thickness and dissimilar material bonding. The thickness of the facet used in this research is about 100  $\mu\text{m}$ , which is ignorable compared to the length of the facet, but the scale down of the wheel without a change of material thickness will cause a collision between adjacent facets. The scale up of the wheel has a problem on dissimilar material adhesion. The adhesive force between the fold line layer with the facet layer is an important factor for maximum payload. However, load is increased by a cubic while adhesive force is increased by a square, and this discrepancy causes a problem. This topic will be discussed in more detail with a payload issue.

The third topic is about the payload. Expanding the range of material selection for the facet and the fold line is an essential requirement for increasing the payload. In this research, a combination of PET and mesh fabric is used, but there are a variety of options for material selection, including carbon reinforced plastic plate, polycarbonate, ABS resin for the facet, and special-purpose fabric such as Aramid fiber, Kevlar for the fold line layer. The important question is how to pattern, align and adhere these materials.

Accurate pattern alignment is critical to maintaining the payload performance consistency. The weak adhesive film was used for the pattern alignment in this research, but this method should be diversified depending on the material. Using a replaceable jig or a soluble dummy plot can be a candidate. Because

the collapse of the wheel is mainly caused by two reasons: material failure and delamination, the adhesive force is also an important factor for payload performance. In this research, the porosity of the mesh fabric increases adhesive force, but it cannot completely prevent the delamination. We will explore better adhesive methods such as plasma etching, welding, sewing and mechanical locking.

Increasing the thickness of the material is a way to increase a payload without material change. But to be folded compactly, a thicker material requires a larger fold line region and it increases the pliability of the structure. In addition, increasing the thickness requires a larger force to deform the wheel. The effect of these conflicting factors is difficult to be analyzed by the kinematic model. The study on this issue needs to be addressed by finite element analysis approach.

Prediction of the effective stiffness and maximum payload of the wheel according to the material properties of the facets and folding parts is important for material selection and design optimization. The kinematic model allows the optimization of the deformation ratio and ensures that the structure has necessary degrees of the freedom, but the stiffness and payload of the wheel cannot be predicted because of the unpredictable behavior of the facets, including the flexible facet regions. Finite element analysis of the structure might be a solution, but it poses its own challenges because the wheel structure is composed of multi-material, has complex geometry and undergoes large deformation. The delamination is also one of the major problem to predict the wheel performance based on finite element analysis approach.

The last topic is the hybrid patterning. We think that the hybrid patterning is one of the unique advantages of the combination of soft robotic design approach

with origami inspired design approach. For our wheel application, most of the parts were patterned, and only two types of facets were used. Local patterning with various types of facets can provide various additional functionalities. For example, some regions can be given highly flexibility while others can be constrained. Facets with appropriate compliance can be used as spring components, not just as rigid components. This design approach could be accomplished not only by varying the materials used but also by applying specific hole patternings. We will investigate this in future work. Balancing the degrees of the freedoms and constraints of origami structures will enlarge the application fields of soft robotics.

## Bibliography

- [1] C. Nie, X. Pacheco Corcho and M. Spenko, "Robots on the move: versatility and complexity in mobile robot locomotion." *IEEE Robotics & Automation Magazine*, vol. 20, no. 4, pp. 72-82, 2013.
- [2] R. A. Brooks, "A robot that walks; emergent behaviors from a carefully evolved network." *Neural computation*, vol. 1, no. 2, pp. 253-262, 1989.
- [3] D. C. Kar, "Design of statically stable walking robot: a review." *Journal of Robotic Systems*, vol. 20, no. 11, pp. 671-686, 2003.
- [4] M. Raibert, K. Blankespoor, G. Nelson, R. Playter and T. Team, "Bigdog, the rough-terrain quadruped robot," *Proceedings of the 17th World Congress*, 2008
- [5] U. Saranli, M. Buehler and D. E. Koditschek, "RHex: A simple and highly mobile hexapod robot." *The International Journal of Robotics Research* vol. 20, no. 7, pp. 616-631, 2001.
- [6] W. Lewinger, C. M. Harley, R. E. Ritzmann, M. S. Branicky and R. D. Quinn, "Insect-like antennal sensing for climbing and tunneling behavior in a biologically-inspired mobile robot," *IEEE International Conference on Robotics and Automation*, 2005.
- [7] P. Birkmeyer, K. Peterson and R. S. Fearing , "DASH: A dynamic 16g hexapedal robot," *IEEE/RSJ International Conference on Intelligent Robots and Systems*, 2009.
- [8] J. B. Jeans, and D. Hong, "IMPASS: Intelligent mobility platform with active spoke system," *IEEE International Conference on Robotics and Automation*, 2009.

- [9] S-C Chen, K-J Huang, W-H Chen, S-Y Shen, C-H Li, P-C Lin, "Quattroped: A Leg--Wheel Transformable Robot," *IEEE/ASME Transactions on Mechatronics*, vol. 19, no. 2, pp. 730-742, 2014
- [10] Y-S Kim, G-P. Jung, H. Kim, K.-J. Cho, C.-N. Chu, "Wheel Transformer: A Wheel-Leg Hybrid Robot With Passive Transformable Wheels," *IEEE Transactions on Robotics* vol. 30, no. 6, pp. 1487-1498, 2014
- [11] K. Nagatani, M. Kuze, K. Yoshida. "Development of transformable mobile robot with mechanism of variable wheel diameter," *Journal of Robotics and Mechatronics*, vol. 19, no. 3, pp. 252-257, 2007.
- [12] Y. She, C. J. Hurd, H. J. Su. "A transformable wheel robot with a passive leg," *IEEE/RSJ International Conference on Intelligent Robots and Systems*, pp. 4165-4170, 2015.
- [13] F. Ilievski, A. D. Mazzeo, R. F. Shepherd, X. Chen, G. M. Whitesides, "Soft robotics for chemists," *Angewandte Chemie International Edition*, vol. 50, no. 8, pp. 1890-1895, 2011.
- [14] S. Kim, C. Laschi, B. Trimmer, "Soft robotics: a bioinspired evolution in robotics. Trends in biotechnology," vol. 31, no. 5, pp. 287-294, 2013
- [15] C. Majidi, "Soft robotics: a perspective—current trends and prospects for the future," *Soft Robotics*, vol. 1, no. 1, pp. 5-11, 2013
- [16] R. F. Shepherd, F. Ilievski, W. Choi, S. A. Morin, A. A. Stokes, A. D. Mazzeo, X. Chen, M. Wang, G. M. Whitesides, "Multigait soft robot," *Proceedings of the National Academy of Sciences*, vol. 108, no. 51, pp. 20400-20403, 2011

- [17] N. W. Bartlett, M. T. Tolley, J. T. Overvelde, J. C. Weaver, B. Mosadegh, K. Bertoldi, G. M. Whitesides and R. J. Wood, "A 3D-printed, functionally graded soft robot powered by combustion," *Science*, vol. 349, no. 6244, pp. 161-165, 2015.
- [18] J. Waynelovich, T. Frey, A. Baljon, P. Salamon, "Versatile and Dexterous Soft Robotic Leg System for Untethered Operations," *Soft Robotics* vol. 3, no. 2, pp. 64-70, 2016
- [19] P. Jackson, *Folding Techniques for Designers: From Sheet to Form*, Pap/Cdr. Laurence King Publishers, 2011.
- [20] R. J. Lang, "The science of origami," *Physics world*, vol. 20, no. 2, p. 30, 2007.
- [21] T. Hull, "On the mathematics of flat origamis", *Congressus Numerantium*, pp. 215–224, 1994.
- [22] K. Miura, "A note on intrinsic geometry of Origami", *Proc. International Meeting on Origami Science and Technology*, Ferrara, Italy, December 6-7, 1989
- [23] E. Demaine, "Origami, linkages, and polyhedra: folding with algorithms", *Algorithms–ESA*, 2006.
- [24] W. Wu, Z. You, "Modelling rigid origami with quaternions and dual quaternions", *Proceedings of the Royal Society A: Mathematical, Physical and Engineering Sciences*, vol. 466, no. 2119, pp. 2155-2174, 2010
- [25] D. Dureisseix, "An overview of mechanisms and patterns with origami," *International Journal of Space Structures*, vol. 27, no. 1, pp. 1-14, 2012

- [26] E. A. Peraza-Hernandez, D. J. Hartl, R. J. Malak RJ, D. C. Lagoudas, "Origami-inspired active structures: a synthesis and review," *Smart Materials and Structures* vol. 23, no. 9: 094001, 2014
- [27] H. Buri, Y. Weinand, "ORIGAMI - Folded Plate Structures, Architecture," *Proceedings of 10th World Conference on Timber Engineering*, 2008.
- [28] T. Tachi, "Geometric Considerations for the Design of Rigid Origami Structures", in *Proc. the International Association for Shell and Spatial Structures Symposium*, 2010.
- [29] M. Schenk and S. D. Guest, "Folded textured sheets", in *Symposium of the International Association for Shell and Spatial Structures*, 2009.
- [30] S. Felton, M. Tolley, E. Demaine, D. Rus, R. Wood, "A method for building self-folding machines," *Science*, vol. 345, no. 6197, pp. 644-646, 2014
- [31] R. V. Martinez, C. R. Fish, X. Chen and G. M. Whitesides, "Elastomeric Origami: Programmable Paper-Elastomer Composites as Pneumatic Actuators", *Advanced Functional Materials*, vol. 22, pp. 1376–1384, 2012.
- [32] E. Hawkes, B. An, N. Benbernou, H. Tanaka, S. Kim, E. Demaine, D. Rus and R. Wood, "Programmable matter by folding", in *Proc. the National Academy of Sciences*, vol. 107, no. 28, p. 12441, 2010.
- [33] J. Koh, and K. Cho, "Omega-shaped Inchworm-inspired Crawling Robot with Large-Index-and-Pitch (LIP) SMA Spring Actuators", *IEEE/ASME Transactions of Mechatronics*, vol. 18, no. 2, pp. 419-429, 2013.



- [34] J. S. Koh, E. Yang, G. P. Jung, S. P. Jung, J. H. Son, S. I. Lee, P. G. Jablonski, R. J. Wood, H. Y. Kim and K. J. Cho, "Jumping on water: Surface tension-dominated jumping of water striders and robotic insects," *Science*, vol. 349, no. 6247, pp. 517-521, 2015
- [35] P. H. Le, Z. Wang and S. Hirai, "Origami structure toward floating aerial robot," *IEEE International Conference on Advanced Intelligent Mechatronics*, pp. 1565-1569, 2015
- [36] J. Ma and Z. You, "Modelling of the waterbomb origami pattern and its applications," *ASME International Design Engineering Technical Conferences DETC2014-35073*, 2014
- [37] K. Kuribayashi, K. Tsuchiya, Z. You, D. Tomus, M. Umemoto, T. Ito, M. Sasaki, "Self-deployable origami stent grafts as a biomedical application of Ni-rich TiNi shape memory alloy foil. Materials," *Science and Engineering* vol. 419, no. 1, pp. 131-137, 2006
- [38] S. Miyashita, S. Guitron, M. Ludersdorfer, C. R. Sung and D. Rus, "An untethered miniature origami robot that self-folds, walks, swims, and degrades," *IEEE International Conference on Robotics and Automation*, pp. 1490-1496, 2015
- [39] N. Bassik, G. M. Stern and D. H. Gracias, "Microassembly based on hands free origami with bidirectional curvature", *Applied physics letters*, Vol. 95, p. 091901, 2009.
- [40] P. O. Vaccaro, K. Kubota, T. Fleischmann, S. Saravanan and T. Aida, "Valley-fold and mountain-fold in the micro-origami technique", *Microelectronics journal*, Vol. 34, No. 5-8, pp. 447-449, 2003.

- [41] D. Lee, J. Koh, J. Kim, S. Kim and K. Cho, "Deformable-wheel robot based on soft material," *International journal of precision engineering and manufacturing*, in Press.
- [42] S. D. Guest and S. Pellegrino, "Inextensional wrapping of flat membranes", in Proc. International Seminar on Structural Morphology, Montpellier, pp 203–215. 1992.
- [43] D.-Y. Lee, G.-P. Jung, M.-K. Sin, S.-H. Ahn, K.-J. Cho, "Deformable wheel robot based on origami structure," *IEEE International Conference on Robotics and Automation*, pp. 5612-5617, 2013
- [44] D.-Y. Lee, J.-S. Kim, J.-J. Park, S.-R. Kim, K.-J. Cho, "Fabrication of origami wheel using pattern embedded fabric and its application to a deformable mobile robot," *IEEE International Conference on Robotics and Automation* pp. 2565-2565, 2014
- [45] D.-Y. Lee, S.-R. Kim, J.-S. Kim, J.-J. Park and K.-J. Cho, "Fabrication of Origami Structure using Pattern Enclosed Composite," *2013 13th International Conference on Control, Automation and Systems*, Oct. 2013

## 국문 초록

# 종이 접기 구조 기반 지름 가변형 휠의 설계 및 제작

바퀴 구동 메커니즘은 간단하고 안정적이며 효율적이지만 정형화되지 않은 지형에서의 이동이 크게 제한된다. 변형 가능한 바퀴를 사용하는 것은 이동형 로봇의 이동성을 증가시키는 주요한 방법 중 하나이다. 바퀴의 반경을 변경함으로써 로봇은 높은 장애물 뿐만 아니라 좁은 틈을 통과할 수 있다.

본 논문은 종이 접기 기반 설계 방식과 소프트 로봇 설계 방식을 복합적으로 활용하여 지름 가변형 바퀴의 새로운 디자인을 제안한다. 소프트 로봇은 부드러운 소재의 무한한 자유도를 바탕으로 고유한 특성 - 높은 자유도의 움직임을 얻는다. 지름 가변형 바퀴에 부드러운 재료를 사용하면 높은 변형성과 충격 흡수 능력이라는 두 가지 장점을 얻을 수 있지만 낮은 강성과 과도한 자유도가 바퀴로서의 기능을 저해하게 된다. 본 논문의 핵심 아이디어는 종이 접기 구조를 인가한 부드러운 소재 기반의 바퀴 구조를 제작하여 이러한 결함을 극복하는 것이다.

제안된 설계는 세 가지 핵심 이점을 제공한다. 첫째, 본 구조는 많은 기계 부품이나 복잡한 조립 공정 없이 제작될 수 있다. 둘째, 종이 접기 구조는 유연한 재료들로 구성되어 전체 구조가 완충 장치 역할을 수행할 수 있기 때문에, 무게에 비해 높은 강성

과 충격 흡수량을 가질 수 있다. 셋째, 종이 접기 구조는 크기 변화에 대한 제약이 작다. 본 구조는 접기에 의해 관절 구조를 생성하므로 링크 사이에 마찰이 거의 존재하지 않는다. 또한 종이 접기 구조를 사용한 단순화 된 조립 공정은 작은 부품을 조립할 때 발생하는 어려움을 줄여 줄 수 있다.

본 논문에서는 새로운 형태의 지름 가변형 바퀴의 설계 및 제조 방법을 제시함과 더불어 바퀴 구조에 대한 해석 및 최적화를 수행하였다. 또한 제안된 구조를 로봇 어플리케이션에 활용하기 위한 변형 메커니즘을 제안하였다. 본 논문에서 제안된 바퀴는 지름의 크기를 30 mm에서 68 mm까지 변형 시킬 수 있으며, 약 9.7g의 가벼운 무게를 가지며, 부드러운 소재로 구성되어 있지만 400 배 이상의 무게를 견딜 수 있다. 제작된 로봇은 지형 조건에 따라 바퀴의 크기를 변경하여 50 mm 크기의 장애물을 넘고 50mm 간격의 틈을 지나갈 수 있었다.

**주요어:** 지름 가변형 바퀴, 종이 접기 구조, 종이 접기 기반 바퀴, 소프트 로봇